

Flow map matching with stochastic interpolants: A unifying framework for consistency models

Anonymous authors

Paper under double-blind review

Abstract

Generative models based on dynamical equations – such as diffusion models and probability flows – offer exceptional sample quality but typically require computationally expensive numerical integration during inference. Recent advances in consistency models have enabled one-step or few-step generation with efficiency comparable to generative adversarial networks; however, despite their practical success, consistency models still lack a unified theoretical framework. Here, we introduce Flow Map Matching (FMM), a principled approach that learns the two-time flow map of an underlying dynamical equation rather than its instantaneous velocity field, thereby providing this missing mathematical foundation. FMM extends the consistency modeling paradigm by allowing practitioners to tune the number of inference steps on the fly, dynamically balancing computational cost and sample quality. By leveraging stochastic interpolants, we propose training objectives both for distillation from a pre-trained velocity field and for direct flow map learning over an interpolant or a forward diffusion process. Theoretically, we show that FMM unifies a range of existing consistency-based approaches, including standard consistency models, consistency trajectory models, and progressive distillation approaches. Experiments on CIFAR-10 and ImageNet 32×32 show that our framework achieves comparable sample quality to flow matching models while reducing generation time by a factor of 10-20.

1 Introduction

In recent years, diffusion models (Song et al., 2020; Ho et al., 2020; Sohl-Dickstein et al., 2015; Song and Ermon, 2020a;b) have achieved state of the art performance across diverse modalities, including image (Dhariwal and Nichol, 2021; Rombach et al., 2022; Esser et al., 2024), audio (Popov et al., 2021; Jeong et al., 2021; Huang et al., 2022; Lu et al., 2022a), and video (Ho et al., 2022a;b; Blattmann et al., 2023; Wu et al., 2023) data. These models belong to a broader class of approaches including flow matching (Lipman et al., 2022), rectified flow (Liu et al., 2022a), and stochastic interpolants (Albergo and Vanden-Eijnden, 2022; Albergo et al., 2023a), which all construct a path in the space of measures between a base and a target distribution by specifying an explicit connection between samples from each (Albergo et al., 2023a). This construction yields a dynamical transport equation governing the evolution of the time-dependent probability measure along the path, which is characterized by a velocity field that must be learned. The generative modeling problem thus reduces to learning this velocity field (Song et al., 2020; Albergo et al., 2023a; Lipman et al., 2022; Liu et al., 2022a), resulting in an efficient and stable training paradigm. At sample generation time, however, models in this class generate data by iteratively converting samples from the base into samples from the target through numerical integration of an ordinary or stochastic differential equation. The number of integration steps required to produce high-quality samples incurs a cost that can limit real-time applications (Chi et al., 2024). Comparatively, one-step models such as GANs (Goodfellow et al., 2014; 2020; Creswell et al., 2018) are notoriously difficult to train (Metz et al., 2017; Arjovsky et al., 2017), but can be hundreds or thousands of times more efficient to sample, because they only require a single network evaluation. Recent efforts have thus focused on maintaining the stable training paradigm of diffusion-type models while reducing the computational burden of sample generation (Karras et al., 2022).

Towards this goal, we introduce Flow Map Matching—a theoretical framework that learns the two-time flow map of a probability flow ODE. Specifically, our primary contributions can be summarized as:

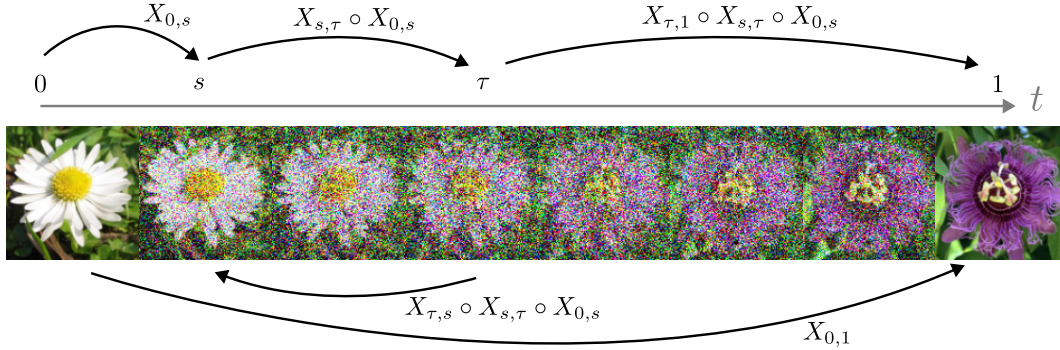


Figure 1: Overview of Flow Map Matching. Our approach learns the two-time flow map $X_{s,t}$ that transports the solution of an ordinary differential equation from time s to time t . Unlike methods that learn instantaneous velocity fields, this bidirectional map can be used to build an integrator with arbitrary discretization. The integrator is exact in theory, and –crucially– its number of steps can be adjusted post-training to balance accuracy and computational efficiency. The flow map can be distilled from a known velocity field or learned directly, and supports arbitrary base distributions, as illustrated here with image-to-image translation.

- We establish formal connections between our framework and recent consistency models (Song et al., 2023; Song and Dhariwal, 2023), consistency trajectory models (Kim et al., 2024a), and their extensions.
- We demonstrate that learning the two-time flow map enables post-training adjustment of sampling steps, allowing practitioners to systematically trade accuracy for computational efficiency - a key advantage over previous approaches.
- We develop a novel *Lagrangian* loss function for distilling a flow map from a pre-trained velocity field, and show that it outperforms a related *Eulerian* loss, which we prove is the continuous-time limit of consistency distillation (Song et al., 2023).
- We show that both the Lagrangian and Eulerian losses control the Wasserstein distance between the teacher and the student models.
- We extend our Lagrangian loss through the stochastic interpolant framework (Albergo and Vanden-Eijnden, 2022; Albergo et al., 2023a), thereby designing a direct training objective for flow map models that eliminates the need for a pre-trained velocity field. We show that this objective provably has the right minimizer, while the loss used for consistency training does not.
- We introduce an efficient map distillation approach inspired by progressive distillation (Salimans and Ho, 2022) and neural operator techniques (Zheng et al., 2023) to convert well-performing few-step maps into equivalent single-step models.

To validate our theoretical framework, we demonstrate its effectiveness via experiments on CIFAR-10 and ImageNet 32×32 , where we achieve high sample quality at significantly reduced computational cost.

2 Related Work

Dynamical transport of measure. Our approach is built upon the modern perspective of generative modeling based on dynamical transport of measure. Grounded in the theory of optimal transport (Villani, 2009; Benamou and Brenier, 2000; Santambrogio, 2015), these models originate at least with (Tabak and Vanden-Eijnden, 2010; Tabak and Turner, 2013), but have been further developed by the machine learning community in recent years (Rezende and Mohamed, 2015; Dinh et al., 2017; Grathwohl et al., 2018; Chen et al., 2019). A breakthrough in this area originated with the appearance of score-based diffusion models (Song et al., 2020; Song and Ermon, 2020a;b), along with related denoising diffusion probabilistic models (Ho et al., 2020; Sohl-Dickstein et al., 2015). These methods generate samples by learning to time-reverse a stochastic differential equation with stationary density given by a Gaussian. More recent approaches such as flow matching (Lipman et al., 2022), rectified flow (Liu et al., 2022a;b), and stochastic interpolants (Albergo

and Vanden-Eijnden, 2022; Albergo et al., 2023a; Ma et al., 2024; Chen et al., 2024) similarly construct connections between the base density and the target, but allow for arbitrary base densities and provide a greater degree of flexibility in the construction of the connection.

Reducing simulation costs. There has been significant recent interest in reducing the cost associated with solving an ODE or an SDE for a generative model based on dynamical transport of measure. One such approach, pioneered by rectification (Liu et al., 2022a;b), is to try to straighten the paths of the probability flow, so as to enable more efficient adaptive integration. In the limit of optimal transport, the paths become straight lines and the integration can be performed in a single step. A second approach is to introduce *couplings* between the base and the target, such as by computing the optimal transport over a minibatch (Pooladian et al., 2023; Tong et al., 2023), or by using data-dependent couplings (Albergo et al., 2023b), which can simplify both training and sampling. A third approach has been to design hand-crafted numerical solvers tailored for diffusion models (Karras et al., 2022; Zhang and Chen, 2023; Jolicœur-Martineau et al., 2021; Liu et al., 2022c; Lu et al., 2022b), or to learn these solvers directly (Watson et al., 2021; 2022; Nichol and Dhariwal, 2021) to maximize efficiency. *Instead, we propose to learn the flow map directly, which avoids estimating optimal transport maps and can overcome the inherent limitations of numerical integration.*

Distillation and consistency techniques. Most related to our approach is a class of one-step models based on *distillation* or *consistency*; we give an explicit mapping between these techniques and our own in Appendix D. Consistency models (Song et al., 2023) have been introduced as a new class of generative models that can either be distilled from a pre-trained diffusion model or trained directly, and are related to several notions of *consistency* of the score model that have appeared in the literature (Lai et al., 2023a;b; Shen et al., 2022; Boffi and Vanden-Eijnden, 2023; Daras et al., 2023). These models learn a one-step map from noise to data, and can be seen as learning a single-time flow map. While they can perform very well, consistency models do not benefit from multistep sampling, and exhibit training difficulties that mandate delicate hyperparameter tuning (Song and Dhariwal, 2023). *By contrast, we learn a two-time flow map, which enables us to smoothly benefit from multistep sampling. Moreover, we introduce new loss functions that are easier to train.* Similarly, neural operator approaches (Zheng et al., 2023) learn a one-time flow map from noise to data, but do so by first generating a dataset of trajectories from the probability flow. Consistency trajectory models (Kim et al., 2024a) were later introduced to improve multistep sampling and to enable the student to surpass the performance of the teacher. Similar to our approach, these models learn a two-time flow map, but do so using a very different loss function that incorporates challenging adversarial training. *Generalized consistency trajectory models (Kim et al., 2024b) extend this approach to the stochastic interpolant setting, but use the original consistency trajectory loss, and do not introduce the Lagrangian perspective considered here. Bidirectional consistency models (Li and He, 2024) learn a two-time invertible flow map similar to our method, but do so in the score-based diffusion setting, and do not leverage our Lagrangian approach; all of these existing consistency models can be seen as a special case of our formalism.* Progressive distillation (Salimans and Ho, 2022) and knowledge distillation (Luhman and Luhman, 2021) techniques aim to convert a diffusion model into an equivalent model with fewer samples by matching several steps of the original diffusion model. This approach is related to our flow map distillation scheme, though the object we distill is fundamentally different.

3 Flow Map Matching

The central object in our method is the *flow map*, which maps points along trajectories of solutions to an ordinary differential equation (ODE). *Our focus in this work is primarily on probability flow ODEs that arise in generative models, such as those constructed using flow matching via stochastic interpolants or score-based diffusion models (see Appendix A for a concise review of these approaches). While many of our results apply more generally to other ODEs, we present our definitions and theoretical results in this specific context to highlight their relevance to generative modeling.* All proofs of the statements made in this section are provided in Appendix B, with some additional theoretical results given in Appendix C.

3.1 Setup and definitions

We consider problems that involve ordinary differential equations (ODEs) defined on \mathbb{R}^d over an ensemble of initial conditions:

$$\dot{x}_t = b_t(x_t), \quad x_{t=0} = x_0 \sim \rho_0, \quad (3.1)$$

where $b : [0, \infty) \times \mathbb{R}^d \rightarrow \mathbb{R}^d$ is the time-dependent velocity field (or drift) and ρ_0 is a base probability density function (PDF) supported on \mathbb{R}^d , which we assume to be positive everywhere.

In generative modeling, equation (3.1) is known as the *probability flow ODE*. Although (3.1) is deterministic for any single trajectory, taken together, its solutions are random because initial conditions are sampled from ρ_0 . We denote by $\rho_t = \text{Law}(x_t)$ the PDF of these solutions at time t .

The key insight in generative modeling is designing (3.1) such that ρ_t evolves from the base density ρ_0 at $t = 0$ to a target density $\rho_T \equiv \rho_*$ at time $T > 0$. This transport is accomplished by learning an appropriate velocity field b_t through methods such as flow matching via stochastic interpolants or score-based diffusion, as detailed in Appendix A. To generate samples from the target density ρ_T , we can then draw initial points from ρ_0 and numerically integrate (3.1) over the interval $t \in [0, T]$. While this approach produces high-quality samples, it typically requires numerous integration steps, making inference computationally expensive—particularly when b_t is parameterized by a complex neural network.

Here, we bypass this numerical integration by estimating the two-time flow map, which we now define under the following assumption.

Assumption 3.1. *The drift satisfies the one-sided Lipschitz condition*

$$\exists C_t \in L^1[0, T] : (b_t(x) - b_t(y)) \cdot (x - y) \leq C_t |x - y|^2 \quad \text{for all } (t, x, y) \in [0, T] \times \mathbb{R}^d \times \mathbb{R}^d. \quad (3.2)$$

Under this assumption, the classical Cauchy-Lipschitz theory (Hartman, 2002) guarantees that solutions of (3.1) exist and are unique for all $x_0 \in \mathbb{R}^d$ and for all $t \in [0, T]$.

Definition 3.2 (Flow Map). *The flow map $X_{s,t} : \mathbb{R}^d \rightarrow \mathbb{R}^d$ for (3.1) is the unique map such that*

$$X_{s,t}(x_s) = x_t \quad \text{for all } (s, t) \in [0, T]^2, \quad (3.3)$$

where $(x_t)_{t \in [0, T]}$ is any solution to the ODE (3.1).

The flow map in Definition 3.2 can be seen as an integrator for (3.1) where the step size $t - s$ may be chosen arbitrarily. In addition to the defining condition (3.3), we now highlight some of its useful properties¹.

Proposition 3.3. *The flow map $X_{s,t}(x)$ is the unique solution to the Lagrangian equation*

$$\partial_t X_{s,t}(x) = b_t(X_{s,t}(x)), \quad X_{s,s}(x) = x, \quad (3.4)$$

for all $(s, t, x) \in [0, T]^2 \times \mathbb{R}^d$. In addition, it satisfies

$$X_{t,\tau}(X_{s,t}(x)) = X_{s,\tau}(x) \quad (3.5)$$

for all $(s, t, \tau, x) \in [0, T]^3 \times \mathbb{R}^d$; in particular $X_{s,t}(X_{t,s}(x)) = x$ for all $(s, t, x) \in [0, T]^2 \times \mathbb{R}^d$, i.e. the flow map is invertible.

Proposition 3.3 shows that if we can draw samples $x_0 \sim \rho_0$, then we can use the flow map to generate one-step samples from ρ_t for any $t \in [0, T]$ exactly via $x_t = X_{0,t}(x_0) \sim \rho_t$. The composition relation (3.5) is the “consistency” property, here stated over two times, that gives consistency models their name (Song et al., 2023). This relation shows that we can also generate samples in multiple steps using $x_{t_k} = X_{t_{k-1}, t_k}(x_{t_{k-1}}) \sim \rho_{t_k}$ for any discretization points (t_0, \dots, t_K) with $t_k \in [0, T]$ and $K \in \mathbb{N}$.

3.2 Distillation of a known velocity field $b_t(x)$

The differential characterization of the flow map given by Proposition 3.3 leads to a distillation loss that can be used to learn an integrator for any differential equation with known right-hand side b , as we now show.

¹We refer to (3.4) as the “Lagrangian equation” because it is defined in a frame of reference that moves with $X_{s,t}(x)$. Later, we write down an alternative “Eulerian” relation that is defined at any fixed point $x \in \mathbb{R}^d$.

Corollary 3.4 (Lagrangian map distillation). *Let $\hat{\rho}_s(x) > 0$ be a family of probability density functions indexed by $s \in [0, T]$, and let $w_{s,t} \in L^1([0, T]^2)$ be a weight function satisfying $w_{s,t} > 0$. Then the flow map is the global minimizer over \hat{X} of the loss*

$$\mathcal{L}_{LMD}(\hat{X}) = \int_{[0, T]^2} \int_{\mathbb{R}^d} w_{s,t} |\partial_t \hat{X}_{s,t}(x) - b_t(\hat{X}_{s,t}(x))|^2 \hat{\rho}_s(x) dx ds dt, \quad (3.6)$$

subject to the boundary condition that $\hat{X}_{s,s}(x) = x$ for all $x \in \mathbb{R}^d$ and $s \in [0, T]$.

Note that (3.6) can be written as an expectation over $\hat{x}_s \sim \hat{\rho}_s$ and $(s, t) \sim w_{s,t}$ (properly normalized):

$$\mathcal{L}_{LMD}(\hat{X}) = \mathbb{E}_{(s,t) \sim w_{s,t}} \mathbb{E}_{\hat{x}_s \sim \hat{\rho}_s} [|\partial_t \hat{X}_{s,t}(\hat{x}_s) - b_t(\hat{X}_{s,t}(\hat{x}_s))|^2]. \quad (3.7)$$

We stress that we can use any density $\hat{\rho}_s(x) > 0$ in (3.6). Nevertheless, it will be convenient to use $\hat{\rho}_s = \rho_s$, as it guarantees that we learn the flow map at values of x where we typically need to evaluate it. Moreover, we will show in Section 3.4 how stochastic interpolants or diffusion models enable us to evaluate (3.6) empirically without having to solve the ODE (3.1) by providing direct access to samples from ρ_s .

For simplicity, Corollary 3.4 is stated for $w_{s,t} > 0$ (e.g. $w_{s,t} = 1$), so that we can estimate the map $X_{s,t}$ and its inverse $X_{t,s}$ for all $(s, t) \in [0, T]$. Nevertheless, this weight can also be adjusted to learn the map for different pairs (s, t) of interest. For example, if we only want to estimate the forward map with $s \leq t$, then we can set $w_{s,t} = 1$ if $s \leq t$ and $w_{s,t} = 0$ otherwise.

When applied to a pre-trained model, such as the b of the probability flow equation of a flow matching or diffusion model, Corollary 3.4 can be used to train a new, few-step generative model with performance that matches that of the teacher. When $\hat{X}_{s,t}$ is parameterized by a neural network, the partial derivative with respect to t can be computed efficiently using forward-mode automatic differentiation in most modern deep learning packages. This procedure is summarized in Algorithm 1.

Equation (3.6) is based on the Lagrangian equation (3.4). The following result shows that the flow map $X_{s,t}$ also obeys an Eulerian equation involving a derivative with respect to s .

Proposition 3.5. *The flow map $X_{s,t}$ is the unique solution of the Eulerian equation*

$$\partial_s X_{s,t}(x) + b_s(x) \cdot \nabla X_{s,t}(x) = 0, \quad X_{t,t}(x) = x, \quad (3.8)$$

for all $(s, t, x) \in [0, T]^2 \times \mathbb{R}^d$.

By squaring the left hand-side of (3.8), we may construct a second loss function for distillation.²

Corollary 3.6 (Eulerian map distillation). *Let $\hat{\rho}_s(x)$ and $w_{s,t}$ be as in Corollary 3.4. Then the flow map is the global minimizer over \hat{X} of the loss*

$$\mathcal{L}_{EMD}(\hat{X}) = \int_{[0, T]^2} \int_{\mathbb{R}^d} w_{s,t} |\partial_s \hat{X}_{s,t}(x) + b_s(x) \cdot \nabla \hat{X}_{s,t}(x)|^2 \rho_s(x) dx ds dt, \quad (3.9)$$

subject to the boundary condition $\hat{X}_{s,s}(x) = x$ for all $x \in \mathbb{R}^d$ and for all $s \in \mathbb{R}$.

Writing (3.9) as an expectation over $\hat{x}_s \sim \hat{\rho}_s$ and $(s, t) \sim w_{s,t}$ gives

$$\mathcal{L}_{EMD}(\hat{X}) = \mathbb{E}_{(s,t) \sim w_{s,t}} \mathbb{E}_{\hat{x}_s \sim \hat{\rho}_s} [|\partial_s \hat{X}_{s,t}(\hat{x}_s) + b_s(\hat{x}_s) \cdot \nabla \hat{X}_{s,t}(\hat{x}_s)|^2]. \quad (3.10)$$

While the Jacobian-vector product $b_s(x) \cdot \nabla \hat{X}_{s,t}(x)$ can be computed using forward-mode automatic differentiation, the high-dimensionality of x in most applications incurs an additional computational expense, so that the loss in Corollary 3.4 may be preferred in practice. In our numerical experiments reported below, we also observed that the loss (3.6) is better behaved and converges faster than (3.9). Nevertheless, we summarize a training procedure based on Corollary 3.6 in Algorithm 2.

²In (3.8), the term $(b_s(x) \cdot \nabla X_{s,t}(x))_i = \sum_{j=1}^d [b_s(x)]_j \partial_{x_j} [X_{s,t}(x)]_i = [\nabla X_{s,t}(x) \cdot b_s(x)]_i$ corresponds to a Jacobian-vector product that can be computed efficiently using forward-mode automatic differentiation.

Algorithm 1 Lagrangian map distillation (LMD)

-
- 1: **Input:** Sampler for the PDF $\hat{\rho}_s(x)$; velocity model b_t ; weight function $w_{s,t}$; batch size M .
 - 2: **repeat**
 - 3: Draw batch $(s_i, t_i, \hat{x}_{s_i})_{i=1}^M$ from $w_{s,t} \times \hat{\rho}_s(x)$.
 - 4: Compute $\hat{\mathcal{L}}_{\text{LMD}} = \frac{1}{M} \sum_{i=1}^M |\partial_t \hat{X}_{s_i, t_i}(\hat{x}_{s_i}) - b_{t_i}(\hat{X}_{s_i, t_i}(\hat{x}_{s_i}))|^2$.
 - 5: Take gradient step on $\hat{\mathcal{L}}_{\text{LMD}}$ to update \hat{X} .
 - 6: **until** converged
 - 7: **Return:** Flow map \hat{X} .
-

Algorithm 2 Eulerian map distillation (EMD)

-
- 1: **Input:** Sampler for the PDF $\hat{\rho}_s(x)$; velocity model b_t ; weight function $w_{s,t}$; batch size M .
 - 2: **repeat**
 - 3: Draw batch $(s_i, t_i, \hat{x}_{s_i})_{i=1}^M$ from $w_{s,t} \times \hat{\rho}_s(x)$.
 - 4: Compute $\hat{\mathcal{L}}_{\text{EMD}} = \frac{1}{M} \sum_{i=1}^M |\partial_s \hat{X}_{s_i, t_i}(\hat{x}_{s_i}) + \nabla \hat{X}_{s_i, t_i}(\hat{x}_{s_i}) b_{t_i}(\hat{x}_{s_i})|^2$.
 - 5: Take gradient step on $\hat{\mathcal{L}}_{\text{EMD}}$ to update \hat{X} .
 - 6: **until** converged
 - 7: **Return:** Flow map \hat{X} .
-

In Appendix D, we demonstrate how the preceding results connect with existing distillation-based approaches. In particular, when $b_t(x)$ is the velocity of the probability flow ODE associated with a diffusion model, Corollary 3.6 recovers the continuous-time limit of the loss functions used for consistency distillation (Song et al., 2023; Song and Dhariwal, 2023) and consistency trajectory models (Kim et al., 2024a), while Corollary 3.4 is new.

3.3 Wasserstein control

In this section, we show that the Lagrangian and Eulerian distillation losses (3.6) and (3.9) control the Wasserstein distance between the density in (A.1) and the density of the pushforward of ρ_0 under the learned flow map. Combined with the Wasserstein bound in Albergo and Vanden-Eijnden (2022), the following results imply a bound on the Wasserstein distance between the target density and the pushforward density for the learned flow map in the case where b is a pre-trained stochastic interpolant or diffusion model. We begin by stating our result for Lagrangian distillation.

Proposition 3.7 (Lagrangian error bound). *Let $X_{s,t} : \mathbb{R}^d \rightarrow \mathbb{R}^d$ denote the flow map for b , and let $\hat{X}_{s,t} : \mathbb{R}^d \rightarrow \mathbb{R}^d$ denote an approximate flow map. Given $x_0 \sim \rho_0$, let $\hat{\rho}_T$ be the PDF of $\hat{X}_{0,T}(x_0)$ and ρ_T be the PDF of $X_{0,T}(x_0)$. Then,*

$$W_2^2(\rho_T, \hat{\rho}_T) \leq e^{T+2} \int_0^T |C_t| dt \int_0^T \mathbb{E} [|\partial_t \hat{X}_{0,t}(x_0) - b_t(\hat{X}_{0,t}(x_0))|^2] dt \leq e^{T+2} \int_0^T |C_t| dt \mathcal{L}_{\text{LMD}}(\hat{X}). \quad (3.11)$$

where C_t is the constant that appears in Assumption 3.1.

The proof is given in Appendix B. We now state an analogous result for the Eulerian case.

Proposition 3.8 (Eulerian error bound). *Let $X_{s,t} : \mathbb{R}^d \rightarrow \mathbb{R}^d$ denote the flow map for b , and let $\hat{X}_{s,t} : \mathbb{R}^d \rightarrow \mathbb{R}^d$ denote an approximate flow map. Given $x_0 \sim \rho_0$, let $\hat{\rho}_T$ be the PDF of $\hat{X}_{0,T}(x_0)$ and let ρ_T be the PDF of $X_{0,T}(x_0)$. Then,*

$$W_2^2(\rho_T, \hat{\rho}_T) \leq e^T \int_0^T \mathbb{E} \left[\left| \partial_s \hat{X}_{s,1}(I_s) + b_s(I_s) \cdot \nabla \hat{X}_{s,1}(I_s) \right|^2 \right] ds \leq e^T \mathcal{L}_{\text{EMD}}(\hat{X}). \quad (3.12)$$

The proof is also given in Appendix B. The result in Proposition 3.8 appears stronger than the result in Proposition 3.7, because it is independent of any Lipschitz constant. Notice however that, unlike (3.11), the bound (3.12) involves the spatial gradient of the map $X_{s,t}$, which may be more difficult to control. In our

numerical experiments, we find the best performance when using the Lagrangian distillation loss, rather than the Eulerian distillation loss. We hypothesize and provide numerical evidence that this originates due to the spatial gradient present in the Eulerian distillation loss; in several cases of interest, the learned map can be singular or nearly singular, so that the spatial gradient is not well defined everywhere. This leads to training difficulties that manifest themselves as fuzzy boundaries on the checkerboard dataset and blurry images on image datasets.

3.4 Direct training with stochastic interpolants

The stochastic interpolant framework, which for the reader's convenience we recall in Appendix A, leads to a new loss function for direct training of flow maps that does not require a pre-trained b . We first give the definition of a stochastic interpolant.

Definition 3.9 (Stochastic Interpolant). *The stochastic interpolant I_t between probability densities ρ_0 and ρ_1 is the stochastic process given by*

$$I_t = \alpha_t x_0 + \beta_t x_1 + \gamma_t z, \quad (3.13)$$

where $\alpha, \beta, \gamma^2 \in C^1([0, 1])$ satisfy $\alpha_0 = \beta_1 = 1$, $\alpha_1 = \beta_0 = 0$, and $\gamma_0 = \gamma_1 = 0$. In (3.13), (x_0, x_1) is drawn from a coupling $(x_0, x_1) \sim \rho(x_0, x_1)$ that satisfies the marginal constraints $\int_{\mathbb{R}^d} \rho(x_0, x_1) dx_0 = \rho_1(x_1)$ and $\int_{\mathbb{R}^d} \rho(x_0, x_1) dx_1 = \rho_0(x_0)$. Moreover, $z \sim \mathcal{N}(0, Id)$ with $z \perp (x_0, x_1)$.

Theorem 3.6 of (Albergo et al., 2023a) (see also Appendix A here for a proof) shows that the stochastic interpolant given in Definition 3.9 specifies an underlying probability flow ODE, as we now recall.

Proposition 3.10 (Probability flow). *For all $t \in [0, 1]$, the PDF of I_t is the same as the PDF of the solution to (3.1) with drift given by*

$$b_t(x) = \mathbb{E}[\dot{I}_t | I_t = x]. \quad (3.14)$$

In (3.14), $\mathbb{E}[\cdot | I_t = x]$ denotes an expectation over the coupling $(x_0, x_1) \sim \rho(x_0, x_1)$ and $z \sim \mathcal{N}(0, I)$ conditioned on the event $I_t = x$.

Moreover, the drift b can be learned efficiently in practice by solving a square loss regression problem (Albergo et al., 2023a)

$$b = \operatorname{argmin}_{\hat{b}} \int_0^1 \mathbb{E}[\hat{b}_t(I_t) - \dot{I}_t]^2 dt, \quad (3.15)$$

where \mathbb{E} denotes an expectation over the coupling $(x_0, x_1) \sim \rho(x_0, x_1)$ and $z \sim \mathcal{N}(0, Id)$.

A canonical choice when $\rho_0 = \mathcal{N}(0, Id)$ considered in Albergo and Vanden-Eijnden (2022) corresponds to $\alpha_t = 1 - t$, $\beta_t = t$, and $\gamma_t = 0$, which recovers flow matching (Lipman et al., 2022) and rectified flow (Liu et al., 2022a). The choice $\alpha_t = 0$, $\beta_t = t$ and $\gamma_t = \sqrt{1 - t^2}$ corresponds to a variance-preserving diffusion model with the **time-rescaling** $t = -\log \tau$ where $\tau \in [0, \infty)$ is the usual diffusion time³. A variance-exploding diffusion model may be obtained by taking $\alpha_t = 0$, $\beta_t = 1$, and $\gamma_t = T - t$ with $t \in [0, T]$ and where $\tau = T - t$ is the usual diffusion time, though this violates the boundary conditions in Definition 3.9. **For more details about the connection between stochastic interpolants and diffusion models, we again refer the reader to Appendix A.**

Given a pre-trained b , we can use the stochastic interpolant framework to evaluate the expectations in the losses (3.6) and (3.9) by leveraging the fact that $I_t \sim \rho_t$. Alternatively, the following result shows how a flow map can be learned *directly* from I_t without the need of a pre-trained model.

Proposition 3.11 (Flow map matching). *The flow map is the global minimizer over \hat{X} of the loss*

$$\mathcal{L}_{FMM}[\hat{X}] = \int_{[0,1]^2} w_{s,t} \left(\mathbb{E}[\|\partial_t \hat{X}_{s,t}(\hat{X}_{t,s}(I_t)) - \dot{I}_t\|^2] + \mathbb{E}[\|\hat{X}_{s,t}(\hat{X}_{t,s}(I_t)) - I_t\|^2] \right) ds dt, \quad (3.16)$$

subject to the boundary condition $\hat{X}_{s,s}(x) = x$ for all $x \in \mathbb{R}^d$ and for all $s \in \mathbb{R}$. In (3.16), $w_{s,t} > 0$ and \mathbb{E} is taken over the coupling $(x_0, x_1) \sim \rho(x_0, x_1)$ and $z \sim \mathcal{N}(0, Id)$.

³Note that $\gamma_0 = 1$ in this case, so that $I_0 = z$

Algorithm 3 Flow map matching (FMM)

-
- 1: **Input:** Interpolant coefficients $\alpha_t, \beta_t, \gamma_t$; weight function $w_{s,t}$; batch size M .
 - 2: **repeat**
 - 3: Draw batch $(s_i, t_i, x_0^i, x_1^i, z_i)_{i=1}^M$ from $w_{s,t} \times \rho(x_0, x_1) \times \mathcal{N}(z; 0, Id)$.
 - 4: Compute $I_{t_i} = \alpha_{t_i} x_0^i + \beta_{t_i} x_1^i + \gamma_{t_i} z_i$ and $\dot{I}_{t_i} = \dot{\alpha}_{t_i} x_0^i + \dot{\beta}_{t_i} x_1^i + \dot{\gamma}_{t_i} z_i$.
 - 5: Compute the loss function

$$\hat{\mathcal{L}}_{\text{FMM}} = \frac{1}{M} \sum_{i=1}^M \left(|\partial_t \hat{X}_{s_i, t_i}(\hat{X}_{t_i, s_i}(I_{t_i})) - \dot{I}_{t_i}|^2 + |\hat{X}_{s_i, t_i}(\hat{X}_{t_i, s_i}(I_{t_i})) - I_{t_i}|^2 \right).$$
 - 6: Take gradient step on $\hat{\mathcal{L}}_{\text{FMM}}$ to update \hat{X} .
 - 7: **until** converged
 - 8: **Return:** Flow map \hat{X} .
-

Algorithm 4 Progressive flow map matching (PFMM)

-
- 1: **Input:** Interpolant coefficients $\alpha_t, \beta_t, \gamma_t$; weight $w_{s,t}$; K -step flow map \hat{X} ; batch size M .
 - 2: **repeat**
 - 3: Draw batch $(s_i, t_i, I_{s_i})_{i=1}^M$ and compute $t_k^i = s_i + (k-1)(t_i - s_i)$ for $k = 1, \dots, K$.
 - 4: Compute $\hat{\mathcal{L}}_{\text{PFMM}} = \frac{1}{M} \sum_{i=1}^M \left(|\check{X}_{s_i, t_i}(I_{s_i}) - (\hat{X}_{t_{K-1}, t_K} \circ \dots \circ \hat{X}_{t_1, t_2})(I_{s_i})|^2 \right)$.
 - 5: Take gradient step on $\hat{\mathcal{L}}_{\text{PFMM}}$ to update \check{X} .
 - 6: **until** converged
 - 7: **Return:** One-step flow map \check{X} .
-

In the loss (3.16), we are free to adjust the weight factor $w_{s,t}$, as illustrated in Figure 2. However, since we need to learn both the map $X_{s,t}$ and its inverse $X_{t,s}$, it is necessary to enforce the symmetry property $w_{t,s} = w_{s,t}$. If we learn the map for all $(s, t) \in [0, 1]^2$ using, for example, $w_{s,t} = 1$, then we can generate samples from ρ_1 in one step via $X_{0,1}(x_0)$ with $x_0 \sim \rho_0$. We note that the second term enforcing invertibility comes at no additional cost, because $\hat{X}_{s,t}(\hat{X}_{t,s}(I_t))$ can be computed at the same time as $\partial_t \hat{X}_{s,t}(\hat{X}_{t,s}(I_t))$ with standard Jacobian-vector product functionality in modern deep learning packages. A summary of the flow map matching procedure is given in Algorithm 3. Empirically, we found learning a one-step map to be challenging in practice. Convergence was significantly improved by taking $w_{s,t} = w_{t,s} = \mathbb{I}(|t - s| \leq 1/K)$ for some $K \in \mathbb{N}$ where \mathbb{I} denotes an indicator function. Given such a K -step model, it can be converted into a one-step model using a map distillation loss that is similar to progressive distillation (Salimans and Ho, 2022) and neural operator approaches (Zheng et al., 2023).

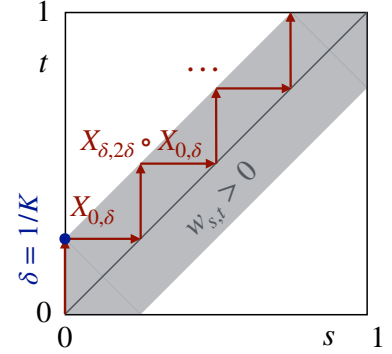


Figure 2: Schematic illustrating the weight $w_{s,t}$ in the FMM loss, which can be tuned to arrive at different learning schemes.

Lemma 3.12 (Progressive flow map matching). *Let \hat{X} be a two-time flow map. Given $K \in \mathbb{N}$, let $t_k = s + (k-1)(t-s)$ for $k = 1, \dots, K$. Then the unique minimizer over \check{X} of the objective*

$$\mathcal{L}_{\text{PFMM}}[\check{X}] = \int_{[0,1]^2} w_{s,t} \mathbb{E} \left[|\check{X}_{s,t}(I_s) - (\hat{X}_{t_{K-1}, t_K} \circ \dots \circ \hat{X}_{t_1, t_2})(I_s)|^2 \right] ds dt, \quad (3.17)$$

produces the same output in one step as the K -step iterated map \hat{X} . Here $w_{s,t} > 0$, and \mathbb{E} is taken over the coupling $(x_0, x_1) \sim \rho(x_0, x_1)$ and $z \sim \mathcal{N}(0, Id)$.

We note that \hat{X} is fixed in (3.17) and serves as the teacher, so we only need to compute the gradient with respect to the parameters of \check{X} . We also note that we only need to learn \check{X} in practice, we may train \hat{X} using (3.16) over a class of neural networks and then freeze its parameters. We may then use (3.17) to distill \hat{X} into a more efficient model \check{X} , which can be initialized from the parameters of \hat{X} for an efficient warm start.

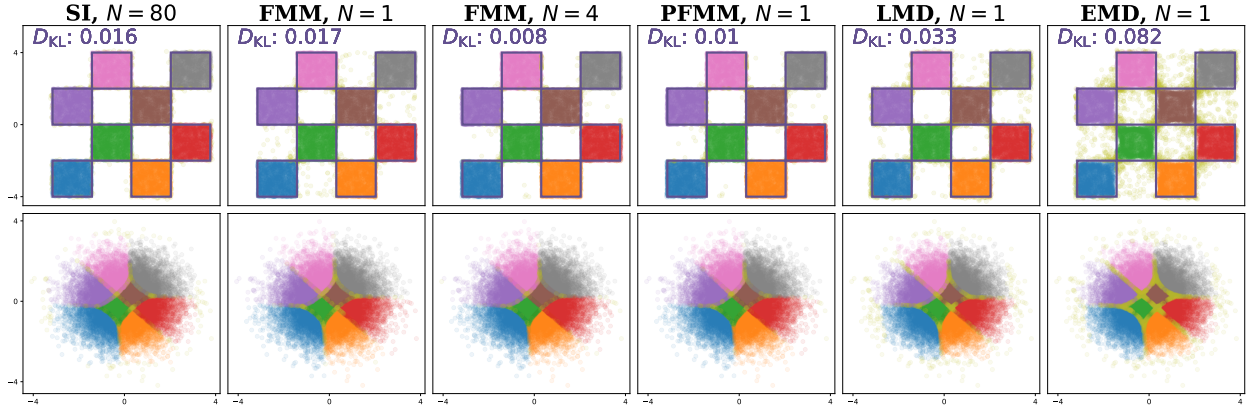


Figure 3: Two-dimensional results. Comparison of the various map-matching procedures on the 2D checkerboard dataset, with the results from the probability flow ODE of a stochastic interpolant integrated using $N = 80$ discretization steps as reference (top, first panel from left). The one-step map obtained by FMM when learning on $(s, t) = [0, 1]^2$ (top, second panel) performs as well as SI. Moreover, the accuracy improves if we allow four steps instead of one (top, third panel). This four-step map can be accurately distilled into a one-step map via PFMM (top, fourth panel). The one-step map obtained by distilling the pre-trained b via LMD (top, fifth panel) performs reasonably well too, and is better than the one-step map obtained by distilling the same b via EMD (top, sixth panel). A KL-divergence between each model distribution and the target is provided to quantify performance, indicating that FMM, its progressive distillation, and LMD are closest to the probability flow ODE baseline. The bottom row indicates, by color, how points from the Gaussian base are assigned by each of the respective maps. The yellow dots are points that mistakenly land outside the checkerboard. These results indicate that the primary source of error in each case is handling the discontinuity of the optimal map at the edges of the checker. See Appendix E for more details.

If the K evaluations of \hat{X} are expensive, we may iteratively minimize (3.17) with some number $M < K$ evaluations of \hat{X} and then replace \hat{X} by \check{X} , similar to progressive distillation (Salimans and Ho, 2022). For example, we may take $M = 2$ and then minimize (3.17) $\lceil \log_2 K \rceil$ times to obtain a one-step map. Alternatively, we can first generate a dataset of $(s, t, I_s, (\hat{X}_{t_{K-1}, t_K} \circ \dots \circ \hat{X}_{t_1, t_2})(I_s))$ in a parallel offline phase, which converts (3.17) into a simple least-squares problem. Finally, if we are only interested in using the map forward in time, we can set $w_{s,t} = 1$ if $s \leq t$ and $w_{s,t} = 0$ otherwise. The resulting procedure is summarized in Algorithm 4.

4 Numerical Realizations

In this section, we study the efficacy of the four methods introduced in Section 3: the Lagrangian map distillation discussed in Corollary 3.4, the Eulerian map distillation discussed in Corollary 3.6, the direct training approach of Proposition 3.11, and the progressive flow map matching approach of Lemma 3.12. We consider their performance on a two-dimensional checkerboard dataset, as well as in the high-dimensional setting of image generation, to highlight differences in their training efficiency and performance.

To ensure that the boundary conditions on the flow map $\hat{X}_{s,t}$ defined in (3.4) are enforced, in all experiments, we parameterize the map using the ansatz

$$X_{s,t}(x) = x + (t - s)f_{s,t}^\theta(x), \quad (4.1)$$

where $f_{s,t}^\theta(x) : [0, T]^2 \times \mathbb{R}^d \rightarrow \mathbb{R}^d$ is a neural network with parameters θ .

4.1 2D Illustration

As a simple illustration of our method, we consider learning the flow map connecting a two-dimensional Gaussian distribution to the checkerboard distribution presented in Figure 3. Note that this example is challenging because the target density is supported on a compact set, and it is discontinuous at the edge of this set. This mapping can be achieved, as discussed in Section 3, in various ways: (a) implicitly, by solving (3.1) with a learned velocity field using stochastic interpolants (or a diffusion model), (b) directly,

Method	N=2		N=4		Baseline
	FID	T-FID	FID	T-FID	
SI	112.42	-	34.84	-	5.53
EMD	48.32	34.19	44.35	30.74	5.53
LMD	7.13	1.27	6.04	1.05	5.53
PFMM	18.35	7.02	11.14	1.52	8.44

Table 1: Comparison of various distillation methods using FID and Teacher-FID metrics on the CIFAR-10 dataset. Note that for PFMM, no velocity model (e.g. from a stochastic interpolant) is needed. It relies solely on the minimization of (3.16) and (3.17). **Baseline indicates the FID of the teacher model (a velocity field for EMD and LMD integrated with an adaptive fifth-order Runge-Kutta scheme, and a flow map for PFMM) against the true data.**

using the flow map matching objective in (3.16), (c) progressively matching the flow map using (3.17), or (d/e) distilling the map using the Eulerian (3.9) or Lagrangian (3.6) losses. In each case, we use a fully connected neural network with 512 neurons per hidden layer and 6 layers to parameterize either a velocity field $\hat{b}_t(x)$ or a flow map $\hat{X}_{s,t}(x)$. We optimize each loss using the Adam (Kingma and Ba, 2017) optimizer for 5×10^4 training iterations. The results are presented in Figure 3, where we observe that using the one-step $\hat{X}_{0,1}(x)$ directly learned by minimizing (3.16) over the entire interval $(s, t) \in [0, 1]^2$ performs worse than learning with $|t - s| < 0.25$ and sampling with 4 steps. With this in mind, we use the 4-step map as a teacher to minimize the PFMM loss, which produces a performant distilled one-step map. We also note that the EMD loss performs worse than the LMD loss when distilling the map from a learned velocity field for a stochastic interpolant.

4.2 Image Generation

Motivated by the above results, we consider a series of image generation experiments on the CIFAR-10 and ImageNet-32 \times 32 datasets. For comparison, we benchmark the method against alternative techniques that seek to lower the number of steps needed to produce samples with stochastic interpolant models, e.g. by straightening the ODE trajectories using minibatch OT (Pooladian et al., 2023; Tong et al., 2023). We train all of our models from scratch, so as to control the design space of the comparison. For clarity, we label when benchmark numbers are quoted from the literature.

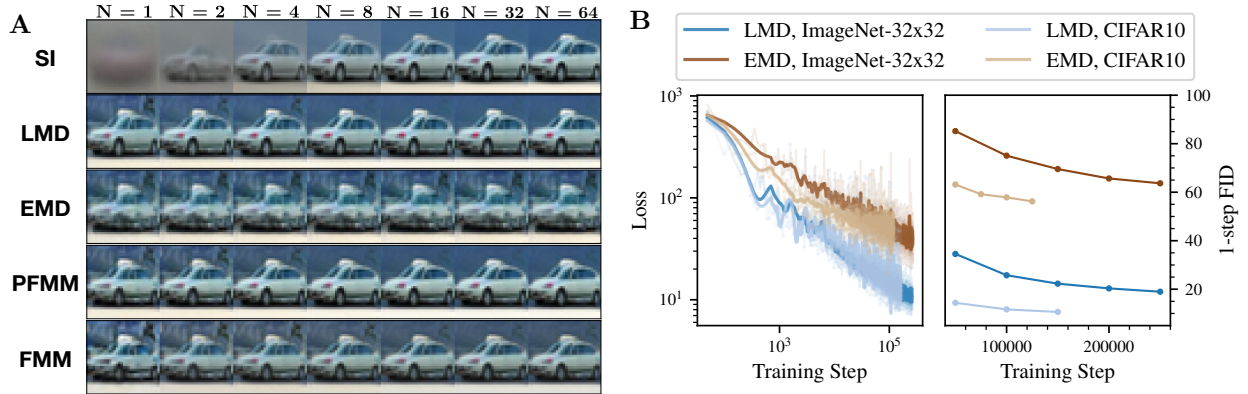


Figure 4: (A) Qualitative comparison between the standard stochastic interpolant approach (SI), Lagrangian map distillation (LMD), Eulerian map distillation (EMD), and progressive flow map matching (PFMM). SI produces good images for a sufficiently large number of steps, but performs poorly for few steps. LMD performs well in the very-few step regime, and outperforms EMD significantly. PFMM performs well at any number of steps, though performs slightly worse than LMD in the very-few step regime. (B) Quantitative comparison between EMD and LMD on both CIFAR-10 and ImageNet 32 \times 32. Despite both having the same minimizer, LMD trains faster, and attains a lower loss value and a lower FID for a fixed number of training steps.

For learning of the flow map, we use a U-Net architecture following (Dhariwal and Nichol, 2021). For LMD and EMD that require a pre-trained velocity field to distill, we also use a U-Net architecture for b . Because the flow map $X_{s,t}$ is a function of two times, we modify the architecture. Both s and t are embedded identically to t in the original architecture. The result is concatenated and treated like t in the original architecture for downstream layers. We benchmark the performance of the methods using the Frechet Inception Distance (FID), which computes a measure of similarity between real images from the dataset and those generated by our models. **In addition, we compute what we denote as the Teacher-FID (T-FID). This metric computes the same measure of similarity, but now between images generated by the teacher model and those generated by the distilled model, rather than leveraging the original dataset. This measure allows us to directly benchmark the convergence of the distillation method, as it captures discrepancies between the distribution of samples generated by the teacher and the distribution of samples generated by the student.** In addition, this allows us to benchmark accuracy independent of the overall performance of the teacher, as our teacher models were trained with limited compute.

Sampling efficiency In Table 1, we compute the FID and T-FID for the stochastic interpolant, Eulerian, Lagrangian, and progressive distillation models on 2 and 4-step generation for CIFAR-10. The stochastic interpolant was trained to a baseline FID (sampling with an adaptive solver) of 5.53, and was used as the teacher for EMD and LMD. The teacher for PFMM was an FMM model trained with $|t - s| < 0.25$ to an FID of 8.44 using 8-step sampling. We observe that LMD and EMD methods can effectively distill their teachers and obtain low T-FID scores. In addition, the 2 and 4-step samples from these methods far outperform the stochastic interpolant. This sampling efficiency is also apparent in the left side of Figure 4, in which with just 1 to 4 steps, the LMD and PFMM methods can produce effective samples, particularly when compared to the flow matching approach.

N	DDPM	BatchOT	FMM (Ours)
20	63.08	7.71	9.68
8	232.97	15.64	12.61
6	275.28	22.08	14.48
4	362.37	38.86	16.90

Table 2: FID scaling with number of function evaluations N to produce a sample on ImageNet- 32×32 . Compares DDPM (Ho et al., 2020) and multi-sample Flow Matching using the BatchOT method (Pooladian et al., 2023) to flow map matching. The first two columns are quoted from Pooladian et al. (2023). Note that no distillation is used here, but rather direct minimization of (3.16), using $|t - s| < 0.25$.

Without any distillation, FMM can also produce effective few-step maps. Training an FMM model on the ImageNet- 32×32 dataset, we observe (Table 2) that FMM achieves much better few-step FID when compared to denoising diffusion models (DDPM), and better FID than mini-batch OT interpolant methods (Pooladian et al., 2023). In the higher-step regime, the interpolant methods perform marginally better.

Eulerian vs Lagrangian distillation Remarkably, we find a stark performance gap between the Eulerian and Lagrangian distillation schemes. This is evident in both parts of Figure 4, where we see that higher-step sampling with EMD only marginally improves image quality, and where the LMD loss for both CIFAR10 and ImageNet- 32×32 converges an order of magnitude faster than the EMD loss. The same holds for FIDs over training, given in the right-most plot in the figure. Note that both LMD and EMD loss functions have a global minimum at 0, so that the loss plots suggest continued training will improve distillation quality, but at very different rates.

4.2.1 Efficient Style Transfer

To highlight some of the downstream tasks facilitated by our approach, we now describe a means of performing style transfer with the two-time invertible flow map that we call “consistency style transfer”. A class conditional sample x_1 with class label y can be partially inverted to an earlier time s' via $X_{1,s'}(x_1; y)$ for $s' < 1$. From here, replacing the class label with $y' \neq y$, we can resample the flow map $X_{s',1}(X_{1,s'}(x_1; y); y')$ to sample the conditional distribution associated to y' while maintaining the style of the original class.

We demonstrate this principle in Figure 5, which shows that maps discretized with $n = 8$ step can be used convert between classes. This serves both as verification of the cycle consistency as well as an illustration of the potential applications of the two-time flow map. In practice, the extent of the preserved style depends on how far back in time towards the Gaussian base at $s' = 0$ we push the original sample. Here, we use $s' = 0.3$.

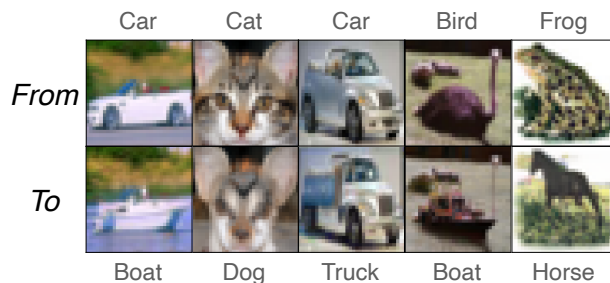


Figure 5: Consistency style transfer on CIFAR-10. Original class-conditional images from the dataset (top row) are pushed backward in time to $X_{1,s'=0.3}(x_1; y)$ and then pushed forward using a new class. The original styles of the images are maintained, while their subjects are replaced with those from the new class (bottom row).

5 Conclusion

In this work, we developed several ways to learn a two-time flow map for generative modeling: either by distilling a pre-trained velocity model with Eulerian or Lagrangian losses, or by directly training with the stochastic interpolant framework. We empirically observe that while using more steps with the learned map improves sample quality, a substantially lower number is needed when compared to other generative models built on dynamical transport. Future work will investigate how to improve the training and the neural network architecture so as to further reduce the number of steps without sacrificing accuracy, and to improve convergence for direct training of one-step maps.

References

- Yang Song, Jascha Sohl-Dickstein, Diederik P Kingma, Abhishek Kumar, Stefano Ermon, and Ben Poole. Score-based generative modeling through stochastic differential equations. *arXiv:2011.13456*, 2020.
- Jonathan Ho, Ajay Jain, and Pieter Abbeel. Denoising diffusion probabilistic models. In *Advances in neural information processing systems*, volume 33, pages 6840–6851, 2020.
- Jascha Sohl-Dickstein, Eric A. Weiss, Niru Maheswaranathan, and Surya Ganguli. Deep unsupervised learning using nonequilibrium thermodynamics. *arXiv:1503.03585*, 2015.
- Yang Song and Stefano Ermon. Improved Techniques for Training Score-Based Generative Models. *arXiv:2006.09011*, October 2020a.
- Yang Song and Stefano Ermon. Generative Modeling by Estimating Gradients of the Data Distribution. *arXiv:1907.05600*, 2020b.
- Prafulla Dhariwal and Alex Nichol. Diffusion Models Beat GANs on Image Synthesis. *arXiv:2105.05233*, 2021.
- Robin Rombach, Andreas Blattmann, Dominik Lorenz, Patrick Esser, and Björn Ommer. High-resolution image synthesis with latent diffusion models. In *Proceedings of the IEEE/CVF conference on computer vision and pattern recognition*, pages 10684–10695, 2022.
- Patrick Esser, Sumith Kulal, Andreas Blattmann, Rahim Entezari, Jonas Müller, Harry Saini, Yam Levi, Dominik Lorenz, Axel Sauer, Frederic Boesel, Dustin Podell, Tim Dockhorn, Zion English, Kyle Lacey, Alex Goodwin, Yannik Marek, and Robin Rombach. Scaling rectified flow transformers for high-resolution image synthesis. *arXiv:2403.03206*, 2024.
- Vadim Popov, Ivan Vovk, Vladimir Gogoryan, Tasnima Sadekova, and Mikhail Kudinov. Grad-TTS: A Diffusion Probabilistic Model for Text-to-Speech. In *Proceedings of the 38th International Conference on Machine Learning*, pages 8599–8608. PMLR, July 2021.
- Myeonghun Jeong, Hyeongju Kim, Sung Jun Cheon, Byoung Jin Choi, and Nam Soo Kim. Diff-TTS: A Denoising Diffusion Model for Text-to-Speech. *arXiv:2104.01409*, 2021.

- Rongjie Huang, Zhou Zhao, Huadai Liu, Jinglin Liu, Chenye Cui, and Yi Ren. ProDiff: Progressive Fast Diffusion Model for High-Quality Text-to-Speech. In *Proceedings of the 30th ACM International Conference on Multimedia*, MM '22, pages 2595–2605, New York, NY, USA, October 2022. Association for Computing Machinery.
- Yen-Ju Lu, Zhong-Qiu Wang, Shinji Watanabe, Alexander Richard, Cheng Yu, and Yu Tsao. Conditional Diffusion Probabilistic Model for Speech Enhancement. In *ICASSP 2022 - 2022 IEEE International Conference on Acoustics, Speech and Signal Processing (ICASSP)*, pages 7402–7406, May 2022a.
- Jonathan Ho, William Chan, Chitwan Saharia, Jay Whang, Ruiqi Gao, Alexey Gritsenko, Diederik P. Kingma, Ben Poole, Mohammad Norouzi, David J. Fleet, and Tim Salimans. Imagen Video: High Definition Video Generation with Diffusion Models. *arXiv:2210.02303*, 2022a.
- Jonathan Ho, Tim Salimans, Alexey Gritsenko, William Chan, Mohammad Norouzi, and David J. Fleet. Video Diffusion Models. *Advances in Neural Information Processing Systems*, 35:8633–8646, December 2022b.
- Andreas Blattmann, Robin Rombach, Huan Ling, Tim Dockhorn, Seung Wook Kim, Sanja Fidler, and Karsten Kreis. Align Your Latents: High-Resolution Video Synthesis With Latent Diffusion Models. *arXiv:2304.08818*, 2023.
- Jay Zhangjie Wu, Yixiao Ge, Xintao Wang, Stan Weixian Lei, Yuchao Gu, Yufei Shi, Wynne Hsu, Ying Shan, Xiaohu Qie, and Mike Zheng Shou. Tune-A-Video: One-Shot Tuning of Image Diffusion Models for Text-to-Video Generation. *arXiv:2212.11565*, 2023.
- Yaron Lipman, Ricky TQ Chen, Heli Ben-Hamu, Maximilian Nickel, and Matthew Le. Flow matching for generative modeling. In *The Eleventh International Conference on Learning Representations*, 2022.
- Xingchao Liu, Chengyue Gong, and Qiang Liu. Flow straight and fast: Learning to generate and transfer data with rectified flow. In *The Eleventh International Conference on Learning Representations*, 2022a.
- Michael S Albergo and Eric Vanden-Eijnden. Building normalizing flows with stochastic interpolants. In *The Eleventh International Conference on Learning Representations*, 2022.
- Michael S Albergo, Nicholas M Boffi, and Eric Vanden-Eijnden. Stochastic interpolants: A unifying framework for flows and diffusions. *arXiv preprint arXiv:2303.08797*, 2023a.
- Cheng Chi, Zhenjia Xu, Siyuan Feng, Eric Cousineau, Yilun Du, Benjamin Burchfiel, Russ Tedrake, and Shuran Song. Diffusion Policy: Visuomotor Policy Learning via Action Diffusion. *arXiv:2303.04137*, 2024.
- Ian Goodfellow, Jean Pouget-Abadie, Mehdi Mirza, Bing Xu, David Warde-Farley, Sherjil Ozair, Aaron Courville, and Yoshua Bengio. Generative Adversarial Nets. In *Advances in Neural Information Processing Systems*, volume 27. Curran Associates, Inc., 2014.
- Ian Goodfellow, Jean Pouget-Abadie, Mehdi Mirza, Bing Xu, David Warde-Farley, Sherjil Ozair, Aaron Courville, and Yoshua Bengio. Generative adversarial networks. *Communications of the ACM*, 63(11): 139–144, October 2020.
- Antonia Creswell, Tom White, Vincent Dumoulin, Kai Arulkumaran, Biswa Sengupta, and Anil A. Bharath. Generative Adversarial Networks: An Overview. *IEEE Signal Processing Magazine*, 35(1):53–65, January 2018.
- Luke Metz, Ben Poole, David Pfau, and Jascha Sohl-Dickstein. Unrolled Generative Adversarial Networks. *arXiv:1611.02163*, 2017.
- Martin Arjovsky, Soumith Chintala, and Léon Bottou. Wasserstein GAN. *arXiv:1701.07875*, 2017.
- Tero Karras, Miika Aittala, Timo Aila, and Samuli Laine. Elucidating the Design Space of Diffusion-Based Generative Models. *arXiv:2206.00364*, 2022.

- Yang Song, Prafulla Dhariwal, Mark Chen, and Ilya Sutskever. Consistency Models. *arXiv:2303.01469*, 2023.
- Yang Song and Prafulla Dhariwal. Improved Techniques for Training Consistency Models. *arXiv:2310.14189*, 2023.
- Dongjun Kim, Chieh-Hsin Lai, Wei-Hsiang Liao, Naoki Murata, Yuhta Takida, Toshimitsu Uesaka, Yutong He, Yuki Mitsufuji, and Stefano Ermon. Consistency Trajectory Models: Learning Probability Flow ODE Trajectory of Diffusion. *arXiv:2310.02279*, 2024a.
- Tim Salimans and Jonathan Ho. Progressive Distillation for Fast Sampling of Diffusion Models. *arXiv:2202.00512*, 2022.
- Hongkai Zheng, Weili Nie, Arash Vahdat, Kamyar Azizzadenesheli, and Anima Anandkumar. Fast Sampling of Diffusion Models via Operator Learning. *arXiv:2211.13449*, 2023.
- Cédric Villani. *Optimal transport: old and new*, volume 338. Springer, 2009.
- Jean-David Benamou and Yann Brenier. A computational fluid mechanics solution to the monge-kantorovich mass transfer problem. *Numerische Mathematik*, 84(3):375–393, 2000.
- Filippo Santambrogio. Optimal transport for applied mathematicians. *Birkhäuser, NY*, 55(58-63):94, 2015.
- Esteban G. Tabak and Eric Vanden-Eijnden. Density estimation by dual ascent of the log-likelihood. *Communications in Mathematical Sciences*, 8(1):217–233, 2010.
- E. G. Tabak and Cristina V. Turner. A family of nonparametric density estimation algorithms. *Communications on Pure and Applied Mathematics*, 66(2):145–164, 2013.
- Danilo Rezende and Shakir Mohamed. Variational Inference with Normalizing Flows. In *International Conference on Machine Learning*, pages 1530–1538. PMLR, June 2015.
- Laurent Dinh, Jascha Sohl-Dickstein, and Samy Bengio. Density Estimation Using Real NVP. In *International Conference on Learning Representations*, page 32, 2017.
- Will Grathwohl, Ricky T. Q. Chen, Jesse Bettencourt, Ilya Sutskever, and David Duvenaud. FFJORD: Free-form Continuous Dynamics for Scalable Reversible Generative Models. *arXiv:1810.01367*, 2018.
- Ricky T. Q. Chen, Yulia Rubanova, Jesse Bettencourt, and David Duvenaud. Neural Ordinary Differential Equations. *arXiv:1806.07366*, 2019.
- Xingchao Liu, Lemeng Wu, Mao Ye, and Qiang Liu. Let us build bridges: Understanding and extending diffusion generative models. *arXiv preprint arXiv:2208.14699*, 2022b.
- Nanye Ma, Mark Goldstein, Michael S. Albergo, Nicholas M. Boffi, Eric Vanden-Eijnden, and Saining Xie. SiT: Exploring Flow and Diffusion-based Generative Models with Scalable Interpolant Transformers. *arXiv:2401.08740*, 2024.
- Yifan Chen, Mark Goldstein, Mengjian Hua, Michael S. Albergo, Nicholas M. Boffi, and Eric Vanden-Eijnden. Probabilistic Forecasting with Stochastic Interpolants and Föllmer Processes. *arXiv:2403.13724*, 2024.
- Aram-Alexandre Pooladian, Heli Ben-Hamu, Carles Domingo-Enrich, Brandon Amos, Yaron Lipman, and Ricky Chen. Multisample flow matching: Straightening flows with minibatch couplings. *arXiv preprint arXiv:2304.14772*, 2023.
- Alexander Tong, Kilian Fatras, Nikolay Malkin, Guillaume Hugué, Yanlei Zhang, Jarrod Rector-Brooks, Guy Wolf, and Yoshua Bengio. Improving and generalizing flow-based generative models with minibatch optimal transport. *Transactions on Machine Learning Research*, 2023.
- Michael S. Albergo, Mark Goldstein, Nicholas M. Boffi, Rajesh Ranganath, and Eric Vanden-Eijnden. Stochastic interpolants with data-dependent couplings. *arXiv:2310.03725*, 2023b.

- Qinsheng Zhang and Yongxin Chen. Fast Sampling of Diffusion Models with Exponential Integrator. *arXiv:2204.13902*, 2023.
- Alexia Jolicœur-Martineau, Ke Li, Rémi Piché-Taillefer, Tal Kachman, and Ioannis Mitliagkas. Gotta Go Fast When Generating Data with Score-Based Models. *arXiv:2105.14080*, 2021.
- Luping Liu, Yi Ren, Zhijie Lin, and Zhou Zhao. Pseudo Numerical Methods for Diffusion Models on Manifolds. *arXiv:2202.09778*, 2022c.
- Cheng Lu, Yuhao Zhou, Jianfei Chen, Chongxuan Li, and Jun Zhu. DPM-Solver: A Fast ODE Solver for Diffusion Probabilistic Model Sampling in Around 10 Steps. *arXiv:2206.00927*, 2022b.
- Daniel Watson, Jonathan Ho, Mohammad Norouzi, and William Chan. Learning to Efficiently Sample from Diffusion Probabilistic Models. *arXiv:2106.03802*, 2021.
- Daniel Watson, William Chan, Jonathan Ho, and Mohammad Norouzi. Learning Fast Samplers for Diffusion Models by Differentiating Through Sample Quality. *arXiv:2202.05830*, 2022.
- Alex Nichol and Prafulla Dhariwal. Improved Denoising Diffusion Probabilistic Models. *arXiv:2102.09672*, 2021.
- Chieh-Hsin Lai, Yuhta Takida, Toshimitsu Uesaka, Naoki Murata, Yuki Mitsufuji, and Stefano Ermon. On the Equivalence of Consistency-Type Models: Consistency Models, Consistent Diffusion Models, and Fokker-Planck Regularization. *arXiv:2306.00367*, 2023a.
- Chieh-Hsin Lai, Yuhta Takida, Naoki Murata, Toshimitsu Uesaka, Yuki Mitsufuji, and Stefano Ermon. Improving Score-based Diffusion Models by Enforcing the Underlying Score Fokker-Planck Equation. *arXiv:2210.04296*, 2023b.
- Zebang Shen, Zhenfu Wang, Satyen Kale, Alejandro Ribeiro, Aim Karbasi, and Hamed Hassani. Self-Consistency of the Fokker-Planck Equation. *arXiv:2206.00860*, 2022.
- Nicholas M. Boffi and Eric Vanden-Eijnden. Probability flow solution of the Fokker-Planck equation. *Machine Learning: Science and Technology*, 4(3):035012, July 2023.
- Giannis Daras, Yuval Dagan, Alexandros G. Dimakis, and Constantinos Daskalakis. Consistent Diffusion Models: Mitigating Sampling Drift by Learning to be Consistent. *arXiv:2302.09057*, 2023.
- Beomsu Kim, Jaemin Kim, Jeongsol Kim, and Jong Chul Ye. Generalized Consistency Trajectory Models for Image Manipulation. *arXiv:2403.12510*, October 2024b.
- Liangchen Li and Jiajun He. Bidirectional Consistency Models. *arXiv:2403.18035*, September 2024.
- Eric Luhman and Troy Luhman. Knowledge Distillation in Iterative Generative Models for Improved Sampling Speed. *arXiv:2101.02388*, January 2021.
- Philip Hartman. *Ordinary Differential Equations*. Society for Industrial and Applied Mathematics, second edition, 2002. doi: 10.1137/1.9780898719222.
- Diederik P. Kingma and Jimmy Ba. Adam: A method for stochastic optimization. *arXiv:1412.6980*, 2017.
- M. Raissi, P. Perdikaris, and G. E. Karniadakis. Physics-informed neural networks: A deep learning framework for solving forward and inverse problems involving nonlinear partial differential equations. *Journal of Computational Physics*, 378:686–707, 2019.
- Jiaming Song, Chenlin Meng, and Stefano Ermon. Denoising Diffusion Implicit Models. *arXiv:2010.02502*, 2022.

A Probability flow ODEs from stochastic interpolants and score-based diffusion models

For the reader’s convenience, we now recall how to construct probability flow ODEs using either flow matching with stochastic interpolants or score-based diffusion models. We also recall the connection between these two formalisms.

A.1 Transport equation

Generative models based on probability flow ODEs leverage the property that solutions to (3.1) push forward their initial conditions onto samples from the target:

Lemma A.1 (Transport equation). *Let $\rho_t = \text{Law}(x_t)$ be the PDF of the solution to (3.1) assuming that $x_0 \sim \rho_0$. Then ρ_t satisfies*

$$\partial_t \rho_t(x) + \nabla \cdot (b_t(x) \rho_t(x)) = 0, \quad \rho_{t=0}(x) = \rho_0(x) \quad (\text{A.1})$$

where ∇ denotes a gradient with respect to x .

The interest of this result is that it can be used in reverse: if we show that a PDF ρ_t satisfies the transport equation (A.1), then in practice we can use the probability flow ODE (3.1) to sample ρ_t at any time $t > 0$, so long as we can sample initial conditions from ρ_0 .

Proof. The proof proceeds via the weak formulation of Equation (A.1). Let $\phi \in C_b^1(\mathbb{R}^d)$ denote an arbitrary test function. By definition,

$$\forall t \in [0, 1] \quad : \quad \int_{\mathbb{R}^d} \phi(x) \rho_t(x) dx = \mathbb{E}[\phi(x_t)] \quad (\text{A.2})$$

where x_t is given by (3.13) and where the expectation on the right hand-side is taken over the law of the initial conditions $x_{t=0} = x_0 \sim \rho_0$. Taking the time derivative of this equality, we deduce that

$$\begin{aligned} \int_{\mathbb{R}^d} \phi(x) \partial_t \rho_t(x) dx &= \mathbb{E}[\dot{x}_t \cdot \nabla \phi(x_t)] && \text{by the chain rule} \\ &= \mathbb{E}[b_t(x_t) \cdot \nabla \phi(x_t)] && \text{using the ODE (3.1)} \\ &= \int_{\mathbb{R}^d} b_t(x) \cdot \nabla \phi(x) \rho_t(x) dx && \text{by definition of } \rho_t(x) \end{aligned} \quad (\text{A.3})$$

This is the weak form of the transport equation (A.1). It can be written as (A.1), since it admits strong solutions by our assumptions on $b_t(x)$. \square

A.2 Stochastic interpolants and probability flows

The stochastic interpolant framework offers a simple and versatile paradigm to construct generative models.

Definition 3.9 (Stochastic Interpolant). *The stochastic interpolant I_t between probability densities ρ_0 and ρ_1 is the stochastic process given by*

$$I_t = \alpha_t x_0 + \beta_t x_1 + \gamma_t z, \quad (\text{3.13})$$

where $\alpha, \beta, \gamma^2 \in C^1([0, 1])$ satisfy $\alpha_0 = \beta_1 = 1$, $\alpha_1 = \beta_0 = 0$, and $\gamma_0 = \gamma_1 = 0$. In (3.13), (x_0, x_1) is drawn from a coupling $(x_0, x_1) \sim \rho(x_0, x_1)$ that satisfies the marginal constraints $\int_{\mathbb{R}^d} \rho(x_0, x_1) dx_0 = \rho_1(x_1)$ and $\int_{\mathbb{R}^d} \rho(x_0, x_1) dx_1 = \rho_0(x_0)$. Moreover, $z \sim \mathcal{N}(0, Id)$ with $z \perp (x_0, x_1)$.

Proposition 3.10 (Probability flow). *For all $t \in [0, 1]$, the PDF of I_t is the same as the PDF of the solution to (3.1) with drift given by*

$$b_t(x) = \mathbb{E}[\dot{I}_t | I_t = x]. \quad (\text{3.14})$$

In (3.14), $\mathbb{E}[\cdot | I_t = x]$ denotes an expectation over the coupling $(x_0, x_1) \sim \rho(x_0, x_1)$ and $z \sim \mathcal{N}(0, I)$ conditioned on the event $I_t = x$.

Proof. Let $\phi \in C_b^1(\mathbb{R}^d)$ denote an arbitrary test function. By definition,

$$\forall t \in [0, 1] \quad : \quad \int_{\mathbb{R}^d} \phi(x) \rho_t(x) dx = \mathbb{E}[\phi(I_t)] \quad (\text{A.4})$$

where I_t is given by (3.13) and where the expectation on the right-hand side is taken over the coupling $(x_0, x_1) \sim \rho(x_0, x_1)$ and $z \sim \mathcal{N}(0, I)$. Taking the time derivative of this equality, we deduce that

$$\begin{aligned} \int_{\mathbb{R}^d} \phi(x) \partial_t \rho_t(x) dx &= \mathbb{E}[\dot{I}_t \cdot \nabla \phi(I_t)] && \text{by the chain rule} \\ &= \mathbb{E}[\mathbb{E}[\dot{I}_t | I_t] \cdot \nabla \phi(I_t)] && \text{by the tower property of the conditional expectation} \\ &= \mathbb{E}[b_t(I_t) \cdot \nabla \phi(I_t)] && \text{by definition of } b_t(x) \text{ in (3.14)} \\ &= \int_{\mathbb{R}^d} b_t(x) \cdot \nabla \phi(x) \rho_t(x) dx && \text{by definition of } \rho_t(x) \end{aligned} \quad (\text{A.5})$$

This is the weak form of the transport equation (A.1). \square

This result implies that the PDF ρ_t of the stochastic interpolant I_t is also the PDF of the solution x_t of the probability flow ODE (3.1) with the velocity field $b_t(x)$ defined in (3.14). Algorithmically, this means that we can use the associated flow map as a generative model.

A.3 Score-based diffusion models

For simplicity, we focus on variance-preserving diffusions; extensions to more general classes of diffusions are straightforward. These models are based on variants of the Ornstein-Uhlenbeck process, defined as the solution to the stochastic differential equation (SDE):

$$dX_t = -X_t dt + \sqrt{2} dW_t, \quad X_{t=0} = a \sim \rho_*, \quad (\text{A.6})$$

where W_t is a Wiener process. The solution to (A.6) for the initial condition $X_{t=0} = a$ is:

$$X_t = a e^{-t} + \sqrt{2} \int_0^t e^{-t+t'} dW_{t'}. \quad (\text{A.7})$$

By the Itô Isometry, the second term on the right-hand side is a Gaussian process with mean zero and covariance given by

$$\mathbb{E} \left[\left(\sqrt{2} \int_0^t e^{-t+t'} dW_{t'} \right)^2 \right] = 2 \text{Id} \int_0^t e^{-2t+2t'} dt' = (1 - e^{-2t}) \text{Id}. \quad (\text{A.8})$$

Therefore, at any time t , the law of (A.7) is that of a Gaussian random variable with mean $a e^{-t}$ and covariance $(1 - e^{-2t}) \text{Id}$. That is, it can be represented as

$$X_t \stackrel{d}{=} a e^{-t} + \sqrt{1 - e^{-2t}} z, \quad (\text{A.9})$$

where $a \sim \rho_*$, $z \sim \mathcal{N}(0, \text{Id})$, and $a \perp z$. (A.9) shows that the law of X_t converges exponentially fast to that of the standard normal variable as $t \rightarrow \infty$ for all initial conditions a .

The key insight of score-based diffusion models is to time-reverse the SDE (A.6) to obtain a process that turns Gaussian samples into samples from the target. Alternatively, this time-reversal can be performed using the associated probability flow ODE. To do so, we can start from the evolution equation for the PDF of the solution to the SDE (A.6). Denoting this PDF by $\tilde{\rho}_t$, it satisfies the Fokker-Planck equation (FPE)

$$\partial_t \tilde{\rho}_t = \nabla \cdot (x \tilde{\rho}_t) + \Delta \tilde{\rho}_t, \quad \tilde{\rho}_0 = \rho_*. \quad (\text{A.10})$$

To time-reverse the solution to (A.10) we define $\rho_t = \tilde{\rho}_{T-t}$ for some large $T > 0$, and derive an equation for ρ_t from (A.10):

$$\begin{aligned} \partial_t \tilde{\rho}_t &= -\partial_t \tilde{\rho}_{T-t} \\ &= -\nabla \cdot (x \tilde{\rho}_{T-t}) - \Delta \tilde{\rho}_{T-t} \\ &= -\nabla \cdot ([x + \nabla \log \tilde{\rho}_{T-t}] \tilde{\rho}_{T-t}) \\ &= -\nabla \cdot ([x + \nabla \log \rho_t] \rho_t) \end{aligned} \quad (\text{A.11})$$

where we used the identity $\Delta \tilde{\rho}_{T-t} = \nabla \cdot (\tilde{\rho}_{T-t} \nabla \log \tilde{\rho}_{T-t})$. Equation (A.11) can be written as

$$\partial_t \tilde{\rho}_t + \nabla \cdot ([x + s_t(x)] \rho_t) = 0, \quad \rho_{t=0} = \tilde{\rho}_{t=T} \approx N(0, \mathbf{I}) \quad (\text{A.12})$$

where $s_t(x) = \nabla \log \rho_t(x) = \nabla \log \tilde{\rho}_{T-t}(x)$ is the score. This quantity can be estimated by regression using the solutions to (A.6), which are explicitly available via (A.9). Equation (A.12) is in the form of (A.1) with a velocity field $b_t(x)$ given by

$$b_t(x) = x + s_t(x). \quad (\text{A.13})$$

Flow map matching can therefore be used to distill score-based diffusion models using this velocity field.

A.4 Connections

Here we show how score-based diffusion models can be related to stochastic interpolants. Recall that the law of the solution to the SDE (A.6) is given by (A.9). If we change time according to $t \mapsto -\log t$, we map $[0, \infty)$ onto $[1, 0)$ and we arrive at

$$X_{-\log t} \stackrel{d}{=} I_t = at + \sqrt{1-t^2}z, \quad a \sim \rho_*, \quad z \sim N(0, \mathbf{I}), \quad \text{and } a \perp z. \quad (\text{A.14})$$

This is a valid stochastic interpolant if we set $a = x_1$, $\beta_t = t$, $\alpha_t = 0$, and $\gamma_t = \sqrt{1-t^2}$ in (3.13)⁴. Hence, we have shown that the probability flow of the score-based diffusion model with velocity field (A.13) can also be studied by using the stochastic interpolant (A.14). Note that this reformulation has the advantage that it eliminates the small bias incurred by the finite value of T in score-based diffusion models, since the stochastic interpolant (A.14) transports the Gaussian random variable z at time $t = 0$ onto the data point a at time $t = 1$ exactly.

B Proofs for Section 3

Proposition 3.3. *The flow map $X_{s,t}(x)$ is the unique solution to the Lagrangian equation*

$$\partial_t X_{s,t}(x) = b_t(X_{s,t}(x)), \quad X_{s,s}(x) = x, \quad (\text{3.4})$$

for all $(s, t, x) \in [0, T]^2 \times \mathbb{R}^d$. In addition, it satisfies

$$X_{t,\tau}(X_{s,t}(x)) = X_{s,\tau}(x) \quad (\text{3.5})$$

for all $(s, t, \tau, x) \in [0, T]^3 \times \mathbb{R}^d$; in particular $X_{s,t}(X_{t,s}(x)) = x$ for all $(s, t, x) \in [0, T]^2 \times \mathbb{R}^d$, i.e. the flow map is invertible.

Proof. Taking the derivative with respect to t of $X_{s,t}(x_s) = x_t$, we deduce

$$\partial_t X_{s,t}(x_s) = \dot{x}_t = b_t(x_t) = b_t(X_{s,t}(x_s)) \quad (\text{B.1})$$

where we used the ODE (3.1) to obtain the second equality. Conversely, since the solutions to (3.1) and (3.4) from a given initial condition are unique, if we solve Equation (3.4) on $[s, t]$ with the condition $X_{s,s}(x_s) = x_s$ we must have $X_{s,t}(x_s) = x_t$ for all $(s, t) \in [0, T]^2$. Evaluating this expression at $x_s = x$ gives (3.4). Also, for all $(s, t, t) \in [0, T]^3$, we have

$$X_{t,t}(X_{s,t}(x_s)) = X_{t,t}(x_t) = x_t = X_{s,t}(x_s). \quad (\text{B.2})$$

Evaluating this expression at $x_s = x$ gives (3.5). \square

Corollary 3.4 (Lagrangian map distillation). *Let $\hat{\rho}_s(x) > 0$ be a family of probability density functions indexed by $s \in [0, T]$, and let $w_{s,t} \in L^1([0, T]^2)$ be a weight function satisfying $w_{s,t} > 0$. Then the flow map is the global minimizer over \hat{X} of the loss*

$$\mathcal{L}_{\text{LMD}}(\hat{X}) = \int_{[0,T]^2} \int_{\mathbb{R}^d} w_{s,t} |\partial_t \hat{X}_{s,t}(x) - b_t(\hat{X}_{s,t}(x))|^2 \hat{\rho}_s(x) dx ds dt, \quad (\text{3.6})$$

subject to the boundary condition that $\hat{X}_{s,s}(x) = x$ for all $x \in \mathbb{R}^d$ and $s \in [0, T]$.

⁴Note that $\gamma_0 = 1$ here, consistent with the fact that the base PDF is Gaussian, so that x_0 and z can be lumped into a single Gaussian variable

Proof. Equation (3.6) is a physics-informed neural network (PINN) (Raissi et al., 2019) loss that is minimized only when the integrand is zero, i.e., when (3.4) holds. \square

Proposition 3.5. *The flow map $X_{s,t}$ is the unique solution of the Eulerian equation*

$$\partial_s X_{s,t}(x) + b_s(x) \cdot \nabla X_{s,t}(x) = 0, \quad X_{t,t}(x) = x, \quad (3.8)$$

for all $(s, t, x) \in [0, T]^2 \times \mathbb{R}^d$.

Proof. Taking the derivative with respect to s of $X_{s,t}(X_{t,s}(x)) = x$ and using the chain rule, we deduce that

$$\begin{aligned} 0 &= \frac{d}{ds} X_{s,t}(X_{t,s}(x)) = \partial_s X_{s,t}(X_{t,s}(x)) + \partial_s X_{t,s}(x) \cdot \nabla X_{s,t}(X_{t,s}(x)) \\ &= \partial_s X_{s,t}(X_{t,s}(x)) + b_s(X_{t,s}(x)) \cdot \nabla X_{s,t}(X_{t,s}(x)) \end{aligned} \quad (B.3)$$

where we used Equation (3.4) to get the last equality. Evaluating this expression at $X_{t,s}(x) = y$, then changing y into x , gives Equation (3.8). \square

Corollary 3.6 (Eulerian map distillation). *Let $\hat{\rho}_s(x)$ and $w_{s,t}$ be as in Corollary 3.4. Then the flow map is the global minimizer over \hat{X} of the loss*

$$\mathcal{L}_{EMD}(\hat{X}) = \int_{[0,T]^2} \int_{\mathbb{R}^d} w_{s,t} |\partial_s \hat{X}_{s,t}(x) + b_s(x) \cdot \nabla \hat{X}_{s,t}(x)|^2 \rho_s(x) dx ds dt, \quad (3.9)$$

subject to the boundary condition $\hat{X}_{s,s}(x) = x$ for all $x \in \mathbb{R}^d$ and for all $s \in \mathbb{R}$.

Proof. Equation (3.9) is a PINN loss that is minimized only when the integrand is zero, i.e., when (3.8) holds. \square

Proposition 3.7 (Lagrangian error bound). *Let $X_{s,t} : \mathbb{R}^d \rightarrow \mathbb{R}^d$ denote the flow map for b , and let $\hat{X}_{s,t} : \mathbb{R}^d \rightarrow \mathbb{R}^d$ denote an approximate flow map. Given $x_0 \sim \rho_0$, let $\hat{\rho}_T$ be the PDF of $\hat{X}_{0,T}(x_0)$ and ρ_T be the PDF of $X_{0,T}(x_0)$. Then,*

$$W_2^2(\rho_T, \hat{\rho}_T) \leq e^{T+2} \int_0^T |C_t| dt \int_0^T \mathbb{E}[|\partial_t \hat{X}_{0,t}(x_0) - b_t(\hat{X}_{0,t}(x_0))|^2] dt \leq e^{T+2} \int_0^T |C_t| dt \mathcal{L}_{LMD}(\hat{X}). \quad (3.11)$$

where C_t is the constant that appears in Assumption 3.1.

Proof. First observe that, by the one-sided Lipschitz condition (3.2),

$$\begin{aligned} \partial_t |X_{s,t}(x) - X_{s,t}(y)|^2 &= 2(X_{s,t}(x) - X_{s,t}(y)) \cdot (b_t(X_{s,t}(x)) - b_t(X_{s,t}(y))), \\ &\leq 2C_t |X_{s,t}(x) - X_{s,t}(y)|^2. \end{aligned} \quad (B.4)$$

Equation (B.4) highlights that (3.2) gives a bound on the spread of trajectories. We note that we allow for $C_t < 0$, which corresponds to globally contracting maps. Given (B.4), we now define

$$E_{s,t} = \mathbb{E}[|X_{s,t}(I_s) - \hat{X}_{s,t}(I_s)|^2], \quad (B.5)$$

where we recall that $X_{s,t}(x)$ satisfies $\partial_t X_{s,t}(x) = b_t(X_{s,t}(x))$ and $X_{s,s}(x) = x$. Taking the derivative with respect to t of (B.5), we deduce

$$\begin{aligned} \partial_t E_{s,t} &= 2\mathbb{E}[(X_{s,t}(I_s) - \hat{X}_{s,t}(I_s)) \cdot (b_t(X_{s,t}(I_s)) - \partial_t \hat{X}_{s,t}(I_s))], \\ &= 2\mathbb{E}[(X_{s,t}(I_s) - \hat{X}_{s,t}(I_s)) \cdot (b_t(\hat{X}_{s,t}(I_s)) - \partial_t \hat{X}_{s,t}(I_s))] \\ &\quad + 2\mathbb{E}[(X_{s,t}(I_s) - \hat{X}_{s,t}(I_s)) \cdot (b_t(X_{s,t}(I_s)) - b_t(\hat{X}_{s,t}(I_s)))], \\ &\leq \mathbb{E}[|X_{s,t}(I_s) - \hat{X}_{s,t}(I_s)|^2] + \mathbb{E}[|b_t(\hat{X}_{s,t}(I_s)) - \partial_t \hat{X}_{s,t}(I_s)|^2] \\ &\quad + 2\mathbb{E}[(X_{s,t}(I_s) - \hat{X}_{s,t}(I_s)) \cdot (b_t(X_{s,t}(I_s)) - b_t(\hat{X}_{s,t}(I_s)))], \\ &\equiv E_{s,t} + \delta_{s,t}^{\text{LMD}} + 2\mathbb{E}[(X_{s,t}(I_s) - \hat{X}_{s,t}(I_s)) \cdot (b_t(X_{s,t}(I_s)) - b_t(\hat{X}_{s,t}(I_s)))]. \end{aligned} \quad (B.6)$$

Above, we defined the two-time Lagrangian distillation error,

$$\delta_{s,t}^{\text{LMD}} = \mathbb{E}[|b_t(\hat{X}_{s,t}(I_s)) - \partial_t \hat{X}_{s,t}(I_s)|^2]. \quad (\text{B.7})$$

By definition, the LMD loss can be expressed as $L_{\text{LMD}}(\hat{X}) = \int_{[0,T]^2} w_{s,t} \delta_{s,t}^{\text{LMD}} ds dt$. Using (3.2) in (B.6), we obtain the relation

$$\partial_t E_{s,t} \leq (1 + 2C_t)E_{s,t} + \delta_{s,t}^{\text{LMD}}, \quad (\text{B.8})$$

which implies that

$$\partial_t (e^{-t-2\int_s^t C_u du} E_{s,t}) \leq e^{-t-2\int_s^t C_u du} \delta_{s,t}^{\text{LMD}}. \quad (\text{B.9})$$

Since $E_{s,s} = 0$ this implies that

$$E_{s,t} \leq \int_s^t e^{(t-u)+2\int_u^t C_t dt} \delta_{s,u}^{\text{LMD}} du \leq e^{t+2\int_s^t |C_t| dt} \int_s^t \delta_{s,u}^{\text{LMD}} du. \quad (\text{B.10})$$

Above, we used that $(t, u) \in [0, t]^2$ so that $(t-u) \leq t$. This bound shows that $E_{0,T} \leq e^{T+2\int_0^T |C_t| dt} \int_0^T \delta_{0,u}^{\text{LMD}} du$, which can be written explicitly as (using t instead of u as dummy integration variable)

$$\mathbb{E}[|X_{0,T}(x_0) - \hat{X}_{0,T}(x_0)|^2] \leq e^{T+2\int_0^T |C_t| dt} \int_0^T \mathbb{E}[|b_t(\hat{X}_{0,t}(x_0)) - \partial_t \hat{X}_{0,t}(x_0)|^2] dt, \quad (\text{B.11})$$

Now, observe that by definition,

$$W_2^2(\rho_T, \hat{\rho}_T) \leq \mathbb{E}[|X_{0,T}(x_0) - \hat{X}_{0,T}(x_0)|^2], \quad (\text{B.12})$$

because the left-hand side is the infimum over all couplings and the right-hand side corresponds to a specific coupling that pairs points from the same initial condition. This completes the proof. \square

Proposition 3.8 (Eulerian error bound). *Let $X_{s,t} : \mathbb{R}^d \rightarrow \mathbb{R}^d$ denote the flow map for b , and let $\hat{X}_{s,t} : \mathbb{R}^d \rightarrow \mathbb{R}^d$ denote an approximate flow map. Given $x_0 \sim \rho_0$, let $\hat{\rho}_T$ be the PDF of $\hat{X}_{0,T}(x_0)$ and let ρ_T be the PDF of $X_{0,T}(x_0)$. Then,*

$$W_2^2(\rho_T, \hat{\rho}_T) \leq e^T \int_0^T \mathbb{E} \left[\left| \partial_s \hat{X}_{s,1}(I_s) + b_s(I_s) \cdot \nabla \hat{X}_{s,1}(I_s) \right|^2 \right] ds \leq e^T \mathcal{L}_{\text{EMD}}(\hat{X}). \quad (3.12)$$

Proof. We first define the error metric

$$E_{s,t} = \mathbb{E} \left[|X_{s,t}(I_s) - \hat{X}_{s,t}(I_s)|^2 \right]. \quad (\text{B.13})$$

It then follows by direct differentiation that

$$\begin{aligned} \partial_s E_{s,t} &= \mathbb{E} \left[2 \left(X_{s,t}(I_s) - \hat{X}_{s,t}(I_s) \right) \cdot \left(\partial_s X_{s,t}(I_s) + \dot{I}_s \cdot \nabla X_{s,t}(I_s) - \left(\partial_s \hat{X}_{s,t}(I_s) + \dot{I}_s \cdot \nabla \hat{X}_{s,t}(I_s) \right) \right) \right], \\ &= \mathbb{E} \left[2 \left(X_{s,t}(I_s) - \hat{X}_{s,t}(I_s) \right) \cdot \left(\partial_s X_{s,t}(I_s) + b_s(I_s) \cdot \nabla X_{s,t}(I_s) - \left(\partial_s \hat{X}_{s,t}(I_s) + b_s(I_s) \cdot \nabla \hat{X}_{s,t}(I_s) \right) \right) \right], \\ &\geq -E_{s,t} - \mathbb{E} \left[\left| \partial_s X_{s,t}(I_s) + b_s(I_s) \cdot \nabla X_{s,t}(I_s) - \left(\partial_s \hat{X}_{s,t}(I_s) + b_s(I_s) \cdot \nabla \hat{X}_{s,t}(I_s) \right) \right|^2 \right], \\ &= -E_{s,t} - \delta_{s,t}^{\text{EMD}}. \end{aligned}$$

Above, we used the tower property of the conditional expectation, the Eulerian equation $\partial_s X_{s,t}(I_s) + b_s(I_s) \cdot \nabla X_{s,t}(I_s) = 0$, and defined the two-time Eulerian distillation error,

$$\delta_{s,t}^{\text{EMD}} = \mathbb{E} \left[\left| \partial_s \hat{X}_{s,t}(I_s) + b_s(I_s) \cdot \nabla \hat{X}_{s,t}(I_s) \right|^2 \right]. \quad (\text{B.14})$$

This implies that

$$\partial_s (-e^s E_{s,t}) \leq e^s \delta_{st}^{\text{EMD}}. \quad (\text{B.15})$$

Using that $E_{t,t} = 0$ for any $t \in [0, T]$ and integrating with respect to s from s to t ,

$$-e^t E_{t,t} + e^s E_{s,t} \leq \int_s^t e^u \delta_{u,t}^{\text{EMD}} du. \quad (\text{B.16})$$

It then follows that

$$E_{s,t} \leq \int_s^t e^{u-s} \delta_{u,t}^{\text{EMD}} du, \quad (\text{B.17})$$

and hence, using that $u - s \in [0, t]$ and that $\delta_{u,t}^{\text{EMD}} \geq 0$,

$$\mathbb{E}[|X_{0,T}(x_0) - \hat{X}_{0,T}(x_0)|^2] \leq e^T \int_0^T \mathbb{E} \left[\left| \partial_s \hat{X}_{s,T}(I_s) + b_s(I_s) \cdot \nabla \hat{X}_{s,T}(I_s) \right|^2 \right] ds. \quad (\text{B.18})$$

The proof is completed upon noting that

$$W_2^2(\rho_T, \hat{\rho}_T) \leq \mathbb{E}[|X_{0,T}(x_0) - \hat{X}_{0,T}(x_0)|^2], \quad (\text{B.19})$$

because the left-hand side is the infimum over all couplings and the right-hand side corresponds to a particular coupling. \square

Proposition 3.11 (Flow map matching). *The flow map is the global minimizer over \hat{X} of the loss*

$$\mathcal{L}_{\text{FMM}}[\hat{X}] = \int_{[0,1]^2} w_{s,t} \left(\mathbb{E}[|\partial_t \hat{X}_{s,t}(\hat{X}_{t,s}(I_t)) - \dot{I}_t|^2] + \mathbb{E}[|\hat{X}_{s,t}(\hat{X}_{t,s}(I_t)) - I_t|^2] \right) ds dt, \quad (\text{3.16})$$

subject to the boundary condition $\hat{X}_{s,s}(x) = x$ for all $x \in \mathbb{R}^d$ and for all $s \in \mathbb{R}$. In (3.16), $w_{s,t} > 0$ and \mathbb{E} is taken over the coupling $(x_0, x_1) \sim \rho(x_0, x_1)$ and $z \sim \mathbf{N}(0, Id)$.

Proof. We start by noticing that

$$\begin{aligned} & \mathbb{E}[|\partial_t \hat{X}_{s,t}(\hat{X}_{t,s}(I_t)) - \dot{I}_t|^2], \\ &= \mathbb{E}[|\partial_t \hat{X}_{s,t}(\hat{X}_{t,s}(I_t))|^2 - 2\dot{I}_t \cdot \partial_t \hat{X}_{s,t}(\hat{X}_{t,s}(I_t)) + |\dot{I}_t|^2], \\ &= \mathbb{E}[|\partial_t \hat{X}_{s,t}(\hat{X}_{t,s}(I_t))|^2 - 2\mathbb{E}[\dot{I}_t | I_t] \cdot \partial_t \hat{X}_{s,t}(\hat{X}_{t,s}(I_t)) + |\dot{I}_t|^2], \\ &= \mathbb{E}[|\partial_t \hat{X}_{s,t}(\hat{X}_{t,s}(I_t))|^2 - 2b_t(I_t) \cdot \partial_t \hat{X}_{s,t}(\hat{X}_{t,s}(I_t)) + |\dot{I}_t|^2], \end{aligned} \quad (\text{B.20})$$

where we used the tower property of the conditional expectation to get the third equality and the definition of $b_t(x)$ in (3.14) to get the last. This means that the loss (3.16) can be written as

$$\begin{aligned} & \mathcal{L}_{\text{FMM}}[\hat{X}] \\ &= \int_{[0,1]^2} \int_{\mathbb{R}^d} w_{s,t} [|\partial_t \hat{X}_{s,t}(\hat{X}_{t,s}(x)) - b_t(x)|^2 + |\hat{X}_{s,t}(\hat{X}_{t,s}(x)) - x|^2] \rho_t(x) dx ds dt \\ &+ \int_{[0,1]^2} w_{s,t} \mathbb{E}[|\dot{I}_t|^2 - |b_t(I_t)|^2] ds dt, \end{aligned} \quad (\text{B.21})$$

where $\rho_t = \text{Law}(I_t)$. The second integral does not depend on \hat{X} , so it does not affect the minimization of $\mathcal{L}_{\text{FMM}}[\hat{X}]$. Assuming that $w_{s,t} > 0$, the first integral is minimized if and only if we have

$$\forall (s, t, x) \in [0, 1]^2 \times \mathbb{R}^d : \quad \partial_t \hat{X}_{s,t}(\hat{X}_{t,s}(x)) = b_t(x) \quad \text{and} \quad \hat{X}_{s,t}(\hat{X}_{t,s}(x)) = x. \quad (\text{B.22})$$

From the second of these equations it follows that: (i) $\hat{X}_{s,s}(x) = x$, and (ii) if we evaluate the first equation at $y = \hat{X}_{t,s}(x)$, this equation reduces to

$$\forall (s, t, y) \in [0, 1]^2 \times \mathbb{R}^d : \quad \partial_t \hat{X}_{s,t}(y) = b_t(\hat{X}_{s,t}(y)) \quad (\text{B.23})$$

which recovers (3.4). \square

Lemma 3.12 (Progressive flow map matching). *Let \hat{X} be a two-time flow map. Given $K \in \mathbb{N}$, let $t_k = s + (k-1)(t-s)$ for $k = 1, \dots, K$. Then the unique minimizer over \hat{X} of the objective*

$$\mathcal{L}_{PFMM}[\hat{X}] = \int_{[0,1]^2} w_{s,t} \mathbb{E} \left[\left| \hat{X}_{s,t}(I_s) - (\hat{X}_{t_{K-1},t_K} \circ \dots \circ \hat{X}_{t_1,t_2})(I_s) \right|^2 \right] ds dt, \quad (3.17)$$

produces the same output in one step as the K -step iterated map \hat{X} . Here $w_{s,t} > 0$, and \mathbb{E} is taken over the coupling $(x_0, x_1) \sim \rho(x_0, x_1)$ and $z \sim \mathcal{N}(0, Id)$.

Proof. Equation (3.17) is a PINN loss whose unique minimizer satisfies

$$\forall (s, t, x) \in [0, T]^2 \times \mathbb{R}^d : \quad \check{X}_{s,t}(x) = (\hat{X}_{t_{K-1},t_K} \circ \dots \circ \hat{X}_{t_1,t_2})(x), \quad (\text{B.24})$$

which establishes the claim. \square

C Additional theoretical results

C.1 Flow maps and denoisers

Since $\text{Law}(X_{t,s}(I_t)) = \text{Law}(I_s)$, it is tempting to replace $X_{t,s}(I_t)$ by I_s in the loss (3.16) and use instead

$$\mathcal{L}_{\text{denoise}}[\hat{X}] = \int_{[0,1]^2} w_{s,t} \mathbb{E} \left[\left| \partial_t \hat{X}_{s,t}(I_s) - \dot{I}_t \right|^2 \right] ds dt, \quad (\text{C.1})$$

minimized over all \hat{X} such that $\hat{X}_{s,s}(x) = x$. However, the minimizer of this objective is *not* the flow map $X_{s,t}$, but rather the denoiser

$$X_{s,t}^{\text{denoise}}(x) = \mathbb{E}[I_t | I_s = x]. \quad (\text{C.2})$$

This can be seen by noticing that the minimizer of (C.1) is the same as the minimizer of

$$\begin{aligned} \mathcal{L}'_{\text{denoise}}[\hat{X}] &= \int_{[0,1]^2} w_{s,t} \mathbb{E} \left[\left| \partial_t \hat{X}_{s,t}(I_s) - \mathbb{E}[\dot{I}_t | I_s] \right|^2 \right] ds dt, \\ &= \int_{[0,1]^2} \int_{\mathbb{R}^d} w_{s,t} \left[\left| \partial_t \hat{X}_{s,t}(x) - \mathbb{E}[\dot{I}_t | I_s = x] \right|^2 \right] \rho_s(x) dx ds dt, \end{aligned} \quad (\text{C.3})$$

which follows from an argument similar to the one used in the proof of Proposition 3.11. The minimizer of (C.3) satisfies

$$\partial_t \hat{X}_{s,t}(x) = \mathbb{E}[\dot{I}_t | I_s = x] = \partial_t \mathbb{E}[I_t | I_s = x], \quad (\text{C.4})$$

which implies (C.2) by the boundary condition $\hat{X}_{s,s}(x) = x$. The denoiser (C.2) may be useful, but it is not a consistent generative model. For instance, if $x_0 \sim \rho_0$ and $x_1 \sim \rho_1$ are independent in the definition of I_t , since $I_0 = x_0$ and $I_1 = x_1$ by construction, for $s = 0$ and $t = 1$ we have

$$X_{0,1}^{\text{denoise}}(x) = \mathbb{E}[x_1] \quad (\text{C.5})$$

i.e. the one-step denoiser only recovers the mean of the target density ρ_1 .

C.2 Eulerian estimation or Eulerian distillation?

In light of the proof of Proposition 3.11, the reader may wonder whether we could also perform direct estimation in the Eulerian setup, using as loss

$$\mathcal{L}_E(\hat{X}) = \int_{[0,T]^2} w_{s,t} \mathbb{E} \left[\left| \partial_s \hat{X}_{s,t}(I_s) + \dot{I}_s \cdot \nabla \hat{X}_{s,t}(I_s) \right|^2 \right] ds dt. \quad (\text{C.6})$$

This loss is obtained from (3.9) by taking the expectation over I_s , using $\text{Law}(I_s) = \rho_s$, and replacing $b_s(I_s)$ by \dot{I}_s . Unfortunately, (C.6) is not equivalent to (3.9). To see why, we can expand the expectation in (C.6):

$$\begin{aligned} &\mathbb{E} \left[\left| \partial_s \hat{X}_{s,t}(I_s) + \dot{I}_s \cdot \nabla \hat{X}_{s,t}(I_s) \right|^2 \right] \\ &= \mathbb{E} \left[\left| \partial_s \hat{X}_{s,t}(I_s) \right|^2 + 2(\dot{I}_s \cdot \nabla \hat{X}_{s,t}(I_s)) \cdot \partial_s \hat{X}_{s,t}(I_s) + \left| \dot{I}_s \cdot \nabla \hat{X}_{s,t}(I_s) \right|^2 \right]. \end{aligned} \quad (\text{C.7})$$

For the cross term (which is linear in \dot{I}_s), we can use the tower property of the conditional expectation to see that

$$\begin{aligned}\mathbb{E}[(\dot{I}_s \cdot \nabla \hat{X}_{s,t}(I_s)) \cdot \partial_s \hat{X}_{s,t}(I_s)] &= \mathbb{E}[(\mathbb{E}[\dot{I}_s | I_s] \cdot \nabla \hat{X}_{s,t}(I_s)) \cdot \partial_s \hat{X}_{s,t}(I_s)], \\ &= \mathbb{E}[(b_s(I_s) \cdot \nabla \hat{X}_{s,t}(I_s)) \cdot \partial_s \hat{X}_{s,t}(I_s)].\end{aligned}\tag{C.8}$$

However, the tower property cannot be applied to the last term in (C.7) since it is quadratic in \dot{I}_t , i.e.

$$\mathbb{E}[(\dot{I}_s \cdot \nabla \hat{X}_{s,t}(I_s))^2] \neq \mathbb{E}[|b_s(I_s) \cdot \nabla \hat{X}_{s,t}(I_s)|^2].\tag{C.9}$$

Since this term depends on \hat{X} , it cannot be neglected in the minimization, and the minimizer of (C.6) is not the same as that of (3.9). Recognizing this difficulty, consistency models (Song et al., 2023; Song and Dhariwal, 2023; Kim et al., 2024a) use a time-discretized variant of (C.6), and place a `stopgrad` on the term $\dot{I}_s \cdot \nabla \hat{X}_{s,t}(I_s)$ when computing the gradient of the loss. The resulting iterative scheme used to update \hat{X} then has a fixed point at $\hat{X} = X$, but it is hard to guarantee that this fixed point is stable and attractive as the iteration is not a gradient descent scheme.

D Relation to existing consistency and distillation techniques

In this section, we recast consistency models and several distillation techniques in the language of our two-time flow map $X_{s,t}$ to clarify their relation with our work.

D.1 Relation to consistency models

Noising process. Following the recommendations in Karras et al. (2022) (which are followed by both Song et al. (2023) and Song and Dhariwal (2023)), we consider the variance-exploding process⁵

$$\tilde{x}_t = a + tz, \quad t \in [0, t_{\max}],\tag{D.1}$$

where $a \sim \rho_1$ (data from the target density) and $z \sim \mathcal{N}(0, I)$. In practice, practitioners often set $t_{\max} = 80$. In this section, because we follow the score-based diffusion convention, we set time so that $t = 0$ recovers ρ_1 and so that a Gaussian is recovered as $t \rightarrow \infty$. The corresponding probability flow ODE is given by

$$\dot{\tilde{x}}_t = -t \nabla \log \rho_t(\tilde{x}_t), \quad \tilde{x}_{t=0} = a \sim \rho_1\tag{D.2}$$

where $\rho_t(x) = \text{Law}(\tilde{x}_t)$. In practice, (D.2) is solved backwards in time from some terminal condition $\tilde{x}_{t_{\max}}$. To make contact with our formulation where time goes forward, we define $x_t = \tilde{x}_{t_{\max}-t}$, leading to

$$\dot{x}_t = (t_{\max} - t) \nabla \log \rho_{t_{\max}-t}(x_t), \quad x_{t=0} \sim \mathcal{N}(x_0, t_{\max}^2 I).\tag{D.3}$$

To make touch with our flow map notation, we then define

$$\partial_t X_{s,t}(x) = (t_{\max} - t) \nabla \log \rho_{t_{\max}-t}(X_{s,t}(x)), \quad X_{s,s}(x) = x.\tag{D.4}$$

Consistency function. By definition (Song et al., 2023), the consistency function $f_t : \mathbb{R}^d \rightarrow \mathbb{R}^d$ is such that

$$f_t(\tilde{x}_t) = a,\tag{D.5}$$

where \tilde{x}_t denotes the solution of (D.2) and $a \sim \rho_1$. To make a connection with our flow map formulation, let us consider (D.5) from the perspective of x_t ,

$$f_t(x_{t_{\max}-t}) = x_{t_{\max}},\tag{D.6}$$

which is to say that

$$f_t(x) = X_{t_{\max}-t, t_{\max}}(x).\tag{D.7}$$

Note that only one time is varied here, i.e. $f_t(x)$, cannot be iterated upon: by its definition (D.5), it always maps the observation \tilde{x}_t onto a sample $a \sim \rho_1$.

⁵Oftentimes $t = 0$ is set to $t = t_{\min} > 0$ for numerical stability, choosing e.g. $t_{\min} = 2 \times 10^{-3}$.

Discrete-time loss function for distillation. In practice, consistency models are typically trained in discrete-time, by discretizing $[t_{\min}, t_{\max}]$ into a set of N points $t_{\min} = t_1 < t_2 < \dots < t_N = t_{\max}$. According to Karras et al. (2022), these points are chosen as

$$t_i = \left(t_{\min}^{1/\eta} + \frac{i-1}{N-1} \left(t_{\max}^{1/\eta} - t_{\min}^{1/\eta} \right) \right)^\eta, \quad (\text{D.8})$$

with $\eta = 7$. Assuming that we have at our disposal a pre-trained estimate $s_t(x)$ of the score $\nabla \log \rho_t(x)$, the *distillation loss* for the consistency function $f_t(x)$ is then given by

$$\begin{aligned} \mathcal{L}_{\text{CD}}^N(\hat{f}) &= \sum_{i=1}^{N-1} \mathbb{E} \left[\left| \hat{f}_{t_{i+1}}(\tilde{x}_{t_{i+1}}) - \hat{f}_{t_i}(\hat{x}_{t_i}) \right|^2 \right], \\ \tilde{x}_{t_{i+1}} &= a + t_{i+1}z \\ \hat{x}_{t_i} &= \tilde{x}_{t_{i+1}} - (t_i - t_{i+1}) t_{i+1} s_{t_{i+1}}(x_{t_{i+1}}), \end{aligned} \quad (\text{D.9})$$

where \mathbb{E} is taken over the data $a \sim \rho_1$ and $z \sim \mathcal{N}(0, I)$. The term \hat{x}_{t_i} is an approximation of \tilde{x}_{t_i} computed by taking a single step of (D.2) with the approximate score model $s_t(x)$. In practice, the square loss in (D.9) can be replaced by an arbitrary metric $d: \mathbb{R}^d \rightarrow \mathbb{R}^d \rightarrow \mathbb{R}_{\geq 0}$, such as a learned metric like LPIPS or the Huber loss.

Continuous-time limit. In continuous-time, it is easy to see via Taylor expansion that the consistency loss reduces to

$$\mathcal{L}_{\text{CD}}^\infty(\hat{f}) = \lim_{N \rightarrow \infty} N \mathcal{L}_{\text{CD}}^N(\hat{f}) = \int_{t_{\min}}^{t_{\max}} \int_{\mathbb{R}^d} w_t^2 \left| \partial_t f_t(x) - t s_t(x) \cdot \nabla f_t(x) \right|^2 \rho_t(x) dx dt, \quad (\text{D.10})$$

where $w_t = \eta(t_{\max}^{1/\eta} - t_{\min}^{1/\eta})t^{1-1/\eta}$ is a weight factor arising from the nonuniform time-grid. This is a particular case of our Eulerian distillation loss (3.9) applied to the variance-exploding setting (D.1) with the identification (D.7).

Estimation vs distillation of the consistency model. If we approximate the exact

$$\nabla \log \rho_t(x) = -\mathbb{E} \left[\frac{\tilde{x}_t - a}{t^2} \middle| \tilde{x}_t = x \right], \quad (\text{D.11})$$

by a single-point estimator

$$\nabla \log \rho_t(x) \approx \frac{a - \tilde{x}_t}{t^2}, \quad (\text{D.12})$$

we may use the expression

$$\hat{x}_{t_i} \approx a + t_i z, \quad (\text{D.13})$$

in (D.9) to obtain the *estimation* loss,

$$\begin{aligned} \mathcal{L}_{\text{CT}}^N(\hat{f}) &= \sum_{i=1}^{N-1} \mathbb{E} \left[\left| \hat{f}_{t_{i+1}}(\tilde{x}_{t_{i+1}}) - \hat{f}_{t_i}^-(\tilde{x}_{t_i}) \right|^2 \right], \\ \tilde{x}_{t_i} &= a + t_i z. \end{aligned} \quad (\text{D.14})$$

This expression does not require a previously-trained score model. Notice, however, that (D.14) must be used with a `stopgrad` on $\hat{f}_{t_i}^-(\tilde{x}_{t_i})$ so that the gradient is taken over only the first $\hat{f}_{t_{i+1}}(\tilde{x}_{t_{i+1}})$. This is because (D.9) and (D.14) are different objectives with different minimizers, even at leading order after expansion in $1/N$, for the same reason that (3.9) differs from (C.6). To see this, observe that to leading order,

$$\hat{f}_{t_i}^-(\tilde{x}_{t_i}) = \hat{f}_{t_{i+1}}^-(\tilde{x}_{t_{i+1}}) + (\partial_t \hat{f}_{t_{i+1}}^-(\tilde{x}_{t_{i+1}}) + z \cdot \nabla \hat{f}_{t_{i+1}}^-(\tilde{x}_{t_{i+1}}))(t_i - t_{i+1}) + O((t_i - t_{i+1})^2), \quad (\text{D.15})$$

which gives the continuous-time limit

$$\mathcal{L}_{\text{CT}}^\infty(\hat{f}) = \lim_{N \rightarrow \infty} \mathcal{L}_{\text{CD}}^N(\hat{f}) = \int_{t_{\min}}^{t_{\max}} \int_{\mathbb{R}^d} w_t \left| \partial_t f_t(x) + z \cdot \nabla f_t^-(x) \right|^2 \rho_t(x) dx dt. \quad (\text{D.16})$$

Observing that $z = \partial_t \tilde{x}_t$ shows that (D.16) recovers the Eulerian estimator described in Appendix C.2, which does not lead to a gradient descent iteration.

	$D_{\text{KL}}(\rho_1 \hat{\rho}_1)$	$W_2^2(\rho_1, \hat{\rho}_1)$	$W_2^2(\hat{\rho}_1^b, \hat{\rho}_1)$	L_2 error
SI	0.020	0.026	0.0	0.000
LMD	0.043	0.059	0.032	0.085
EMD	0.079	0.029	0.010	0.011
FMM, $N = 1$	0.104	0.021	–	0.026
FMM, $N = 4$	0.045	0.014	–	0.024
PFMM, $N = 1$	0.043	0.014	–	0.023

Table 3: Comparison of $D_{\text{KL}}(\rho || \hat{\rho})$ and $W_2^2(\rho, \hat{\rho})$, where $\hat{\rho}$ is the pushforward density from the maps $\hat{X}_{0,1}(x_0)$ for the methods listed above. Additionally included is a comparison of L_2 expected error of the distillation methods against their teacher $\hat{X}_{0,1}^{\text{SI}}$ given as $\mathbb{E}[|\hat{X}_{0,1}^{\text{SI}}(x) - \hat{X}_{0,1}(x)|^2]$. Intriguingly, LMD performs better in being distributionally correct, as measured by the KL-divergence, but worse in preserving the coupling of the teacher model. The roles are flipped for EMD. This may highlight KL as a more informative metric in our case, as our aims are to sample correctly in distribution. See Figure 6 for a visualization.

D.2 Relation to neural operators

In our notation, neural operator approaches for fast sampling of diffusion models (Zheng et al., 2023) also estimate the flow map $X_{0,t}$ via the loss

$$\mathcal{L}_{\text{FNO}}(\hat{X}) = \int_0^1 \int_{\mathbb{R}^d} |\hat{X}_{0,t}(x) - X_{0,t}(x)|^2 \rho_0(x) dx dt, \quad (\text{D.17})$$

where $\hat{X}_{0,t}$ is parameterized by a Fourier Neural Operator and where $X_{0,t}$ is the flow map *obtained by simulating the probability flow ODE associated with a pre-trained (or given) $b_t(x)$* . To avoid simulation at learning time, they pre-generate a dataset of trajectories, giving access to $X_{0,t}(x)$ for many initial conditions $x \sim \rho_0$. Much of the work focuses on the architecture of the FNO itself, which is combined with a U-Net.

D.3 Relation to progressive distillation

Progressive distillation (Salimans and Ho, 2022) takes a DDIM sampler (Song et al., 2022) and trains a new model to approximate two steps of the old sampler with one step of the new model. This process is iterated repeatedly to successively halve the number of steps required. In our notation, this corresponds to minimizing

$$\mathcal{L}_{\text{PD}}^{\Delta t}(\hat{X}) = \int_0^{1-2\Delta t} \int_{\mathbb{R}^d} |\hat{X}_{t,t+2\Delta t}(x) - (X_{t+\Delta t,t+2\Delta t} \circ X_{t,t+\Delta t})(x)|^2 \rho_t(x) dx dt \quad (\text{D.18})$$

where X is a pre-trained map from the previous iteration. This is then iterated upon, and Δt is increased, until what is left is a few-step model.

E Additional Experimental Details

E.1 2D checkerboard

Here, we provide further discussion and analysis of our results for generative modeling on the 2D checkerboard distribution (Figure 3). Our KL-divergence estimates clearly highlight that there is a hierarchy of performance. Of particular interest is the large discrepancy in performance between the Eulerian and Lagrangian distillation techniques.

As noted in Figure 3 and Table 3, LMD substantially outperforms its Eulerian counterpart in terms of minimizing the KL-divergence between the target checkerboard density ρ_1 and model density $\hat{\rho}_1 = \hat{X}_{0,1} \# \rho_0$. Interestingly, while LMD is more correct in distribution, EMD better preserves the original coupling $(x_0, \hat{X}_{0,1}^{\text{SI}}(x_0))$ of the teacher model $\hat{X}_{0,1}^{\text{SI}}$, as measured by the W_2^2 distance and the expected L_2 reconstruction error, defined as $\mathbb{E}[|\hat{X}_{0,1}^{\text{SI}}(x) - \hat{X}_{0,1}(x)|^2]$. Where this coupling is significantly *not* preserved is visualized in Figure 6. For each model, we color code points for which $|\hat{X}_{0,1}^{\text{SI}}(x) - \hat{X}_{0,1}(x)|^2 > 1.0$, highlighting where the student map differed from the teacher. We notice that the LMD map pushes initial conditions to an opposing checker edge (purple) than where those initial conditions are pushed by the interpolant (blue). This is much less common for the EMD map, but its performance is overall worse in matching the target distribution.

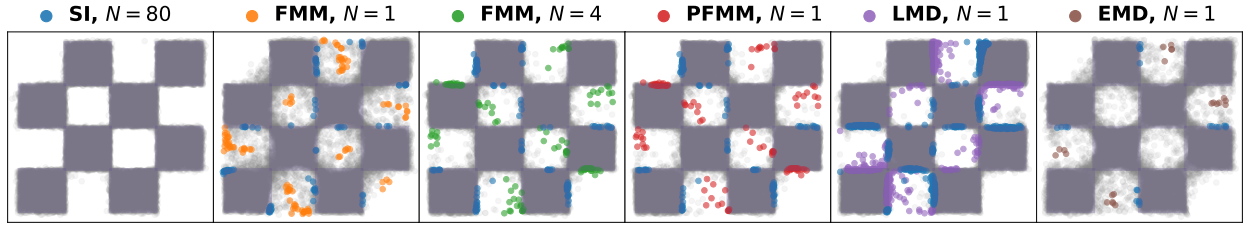


Figure 6: Visualization of the difference in assignment of the maps $\hat{X}_{0,1}(x_0)$ for the various models as compared to the teacher/ground truth model $\hat{X}_{0,1}^{SI}(x_0)$ for the same initial conditions from the base distribution x_0 . Points that lie in the region $|\hat{X}_{0,1}^{SI}(x_0) - \hat{X}_{0,1}(x_0)|^2 > 1.0$ are colored as compared to the blue points, which represent where the stochastic interpolant teacher mapped the same red initial conditions. This gives us an intuition for how well each method precisely maintains the coupling $(x_0, \hat{X}_{0,1}^{SI}(x_0))$ from the teacher. Note that we are treating $X_{0,1}^{SI}$ as the ground truth map here, as it is close to the exact map. The models based on FMM either don't have a teacher or have FMM, $N = 4$ as a teacher, but all should have the same coupling at the minimizer.

E.2 Image experiments

Here we include more experimental details for reproducing the results provided in Section 4. We use the U-Net from the diffusion OpenAI paper (Dhariwal and Nichol, 2021) with code given at <https://github.com/openai/guided-diffusion>. We use the same architecture for both CIFAR10 and ImageNet- 32×32 experiments. The architecture is also the same for training a velocity field and for training a flow map, barring the augmentation of the time-step embedding in the U-Net to handle two times (s, t) instead of one. Details of the training conditions are presented in Table 4.

	CIFAR-10	ImageNet 32×32
Dimension	32×32	32×32
# Training point	5×10^4	1,281,167
Batch Size	256	256
Training Steps (Lagrangian distillation)	1.5×10^5	2.5×10^5
Training Steps (Eulerian distillation)	1.2×10^5	2.5×10^5
Training Steps (Flow map matching)	N/A	1×10^5
Training Steps (Progressive flow map matching)	1.3×10^5	N/A
U-Net channel dims	256	256
Learning Rate (LR)	0.0001	0.0001
LR decay (every 1k epochs)	0.992	0.992
U-Net dim mult	[1,2,2,2]	[1,2,2,2]
Learned time embedding	Yes	Yes
# GPUs	4	4

Table 4: Hyperparameters and architecture for image datasets.